From Nanoscale Design to Functional Integration of Magnetic Nanoparticle Assemblies

A Gas-Phase Strategy

Sedrpooshan, Mehran

2025

Document Version:
Publisher's PDF, also known as Version of record

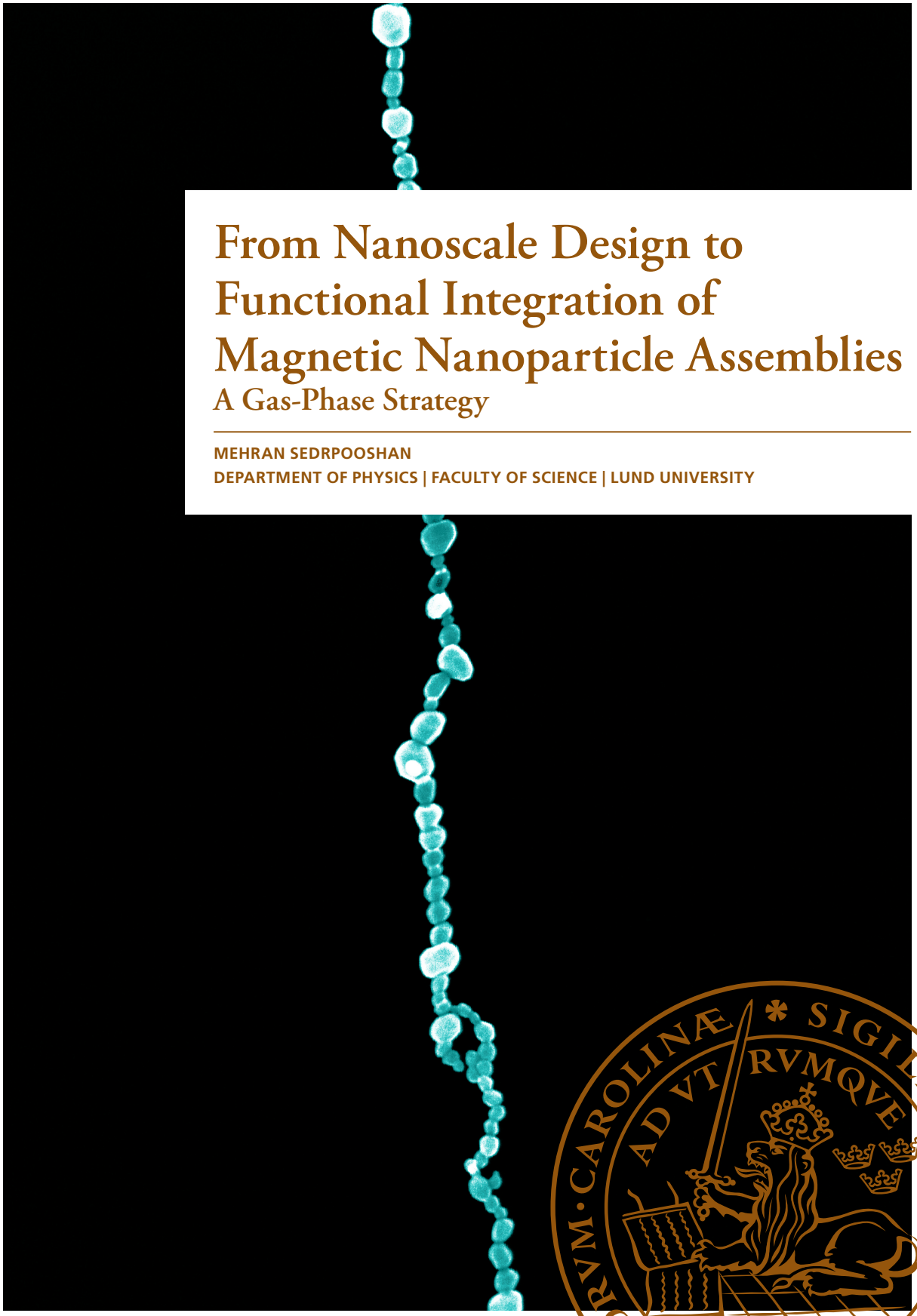

From Nanoscale Design to Functional Integration of Magnetic Nanoparticle Assemblies

A Gas-Phase Strategy

MEHRAN SEDRPOOSHAN
DEPARTMENT OF PHYSICS | FACULTY OF SCIENCE | LUND UNIVERSITY

From Nanoscale Design to Functional Integration of Magnetic Nanoparticle Assemblies

A Gas-Phase Strategy

From Nanoscale Design to Functional Integration of Magnetic Nanoparticle Assemblies

A Gas-Phase Strategy

by Mehran Sedrpooshan

LUND
UNIVERSITY

Doctoral Dissertation
Thesis advisor: Assoc. Prof. Rasmus Westerström
Faculty opponent: Prof. Harald Brune,
École Polytechnique Fédérale de Lausanne (EPFL)

Doctoral dissertation for the degree of Doctor of Philosophy (PhD) at the Faculty of Science at Lund University to be publicly defended on 5th of June 2025 at 9:00 in Rydberg Lecture Hall, Department of Physics, Sölvegatan 14, Lund, Sweden.

Organization
LUND UNIVERSITY

Department of Physics
Box 118
SE–221 00 LUND
Sweden

Document name
DOCTORAL DISSERTATION

Date of disputation
2025-06-05

Sponsoring organization

Author(s)
Mehran Sedrpooshan

Title and subtitle
From Nanoscale Design to Functional Integration of Magnetic Nanoparticle Assemblies: A Gas-Phase Strategy

Abstract

The self-assembly of magnetic nanoparticles under external magnetic fields holds great potential for the facile fabrication of functional magnetic components with a wide range of applications. This work employs a technique based on electrically charged gas-phase magnetic nanoparticles, demonstrating an additional level of control when forming one-dimensional assemblies, so-called nanochains, as an electric field can be used in addition to the magnetic field during the deposition process. This dissertation covers the entire process, from generating charged gas-phase magnetic nanoparticles with different compositions and tuning their assembly process through electric fields to their direct integration onto desired substrates, developing practical applications, and conducting detailed experimental and computational magnetic characterizations and analysis. This work shows that the interplay of the electric and magnetic fields during the deposition process enables the tuning of the spatial distribution of structures on the surface. Furthermore, it demonstrates that this approach facilitates control over the composition of nanoparticles and supports the sequential deposition of different material systems onto each other. Utilizing the direct integration capability of this method, this thesis showcases the creation of magnetically responsive soft films and nanoscale magnetoresistive devices. Finally, the magnetic properties of the fabricated structures are characterized in detail. A combination of magnetometry protocols is used to characterize the structures from an ensemble-averaged perspective. In addition, X-ray microscopy, nanochain devices, and micromagnetic simulations are used to study the structures from a single nanochain point of view.

Key words
spark ablation, aerosol nanoparticles, magnetic nanoparticles, nanoparticle self-assembly, magnetic soft films, magnetoresistive devices, nanomagnetism, magnetization reversal, STXM-XMCD

Classification system and/or index terms (if any)

Supplementary bibliographical information

Language
English

ISSN and key title

ISBN
978-91-8104-519-2 (print)
978-91-8104-520-8 (pdf)

Recipient's notes

Number of pages
168

Price

Security classification

Signature

Date 2025-04-23

From Nanoscale Design to Functional Integration of Magnetic Nanoparticle Assemblies

A Gas-Phase Strategy

by Mehran Sedrpooshan

LUND
UNIVERSITY

Cover illustration front: Modified electron microscopy image of a Co nanochain.

Funding information: The thesis work was financially supported by the European Union's H2020 MSCA (GenerationNano), the Swedish Research Council, the Swedish Energy Agency, the Crafoord Foundation, and NanoLund.

Faculty of Science, Department of Physics

ISBN: 978-91-8104-519-2 (print)
ISBN: 978-91-8104-520-8 (pdf)

Printed in Sweden by Media-Tryck, Lund University, Lund 2025

To the brave women of Iran, whose courage and persistence in the quest for freedom are truly admirable. Especially to my better half, Elham, whose thoughts and strength continue to inspire me.

Contents

List of publications

This thesis is based on the following publications. The papers are referred to in the text by their Roman numerals:

I **Template-free generation and integration of functional 1D magnetic nanostructures**
M. Sedrpooshan, C. Bulbucan, P. Ternero, P. Maltoni, C. Preger, S. Finizio, B. Watts, D. Peddis, A. M. Burke, M. E. Messing, R. Westerström
Nanoscale, 2023, 15 (45), 18500-18510,
DOI: 10.1039/D3NR03878E

II **Single-step generation of 1D FeCo nanostructures**
M. Sedrpooshan, P. Ternero, C. Bulbucan, A. M. Burke, M. E. Messing, R. Westerström
Nano Express, 2024, 5 (2), 025008,
DOI: 10.1088/2632-959X/ad3e1c

III **Effect of the carrier gas on the structure and composition of Co–Ni bimetallic nanoparticles generated by spark ablation**
P. Ternero, **M. Sedrpooshan**, D. Wahlqvist, B. O. Meuller, M. Ek, J. Hübner, R. Westerström, M. E. Messing
Journal of Aerosol Science, 2023, 170, 106146,
DOI: 10.1016/j.jaerosci.2023.106146

IV **Facile morphology and composition control of self-assembled structures by charged gas-phase magnetic nanoparticles**
M. Sedrpooshan, A. Omelyanchik, P. Ternero, C. Bulbucan, P. Maltoni, D. Peddis, A. M. Burke, M. E. Messing, R. Westerström
In manuscript

V **Single-step production and self-assembly of magnetic nanostructures for magneto-responsive soft films**
M. Sedrpooshan, P. Maltoni, D. Peddis, A. M. Burke, M. E. Messing, R. Westerström
ACS Applied Materials & Interfaces, 2025, 17 (14), 21682,
DOI: 10.1021/acsami.5c00992

VI **Direct device integration of single 1D nanoparticle assemblies; A magnetization reversal and magnetotransport study**
M. Sedrpooshan, C. Bulbucan, D. J. Carrad, T. S. Jespersen, A. M. Burke, M. E. Messing, R. Westerström
Nanotechnology, 2025, 36, 185601,
DOI: 10.1088/1361-6528/adc1d0

All papers are reproduced with the permission of their respective publishers.

Papers that I have contributed to during my PhD but are not included in this thesis:

VII **Tunable synthesis and magnetic properties of Co–Ni nanoparticles: from high-coercivity metallic to exchange-biased Janus nanostructures**
P. Ternero, **M. Sedrpooshan**, D. Wahlqvist, B. Bozzo, A. Palau, A. Kovács, R. E. Dunin- Borkowski, M. Ek, R. Westerström, and M. E. Messing
In manuscript

VIII **Tunable Magnetic Environment at the SoftiMAX Beamline**
C. Bulbucan, I. Beinik, J. Schwenke, L. Roslund, **M. Sedrpooshan**, R. Westerström, J. Brandão, I. Neckel, K. Thånell
In submission

IX **In-flight observation and surface oxidation modification of tin oxide nanoparticles for gas sensing applications**
C. Preger, L. Jönsson, P. Ternero, **M. Sedrpooshan**, M. Bermeo Vargas, A. Kivimäki, N. Walsh, M. Messing, A. Eriksson, J. Rissler
ACS Applied Nano Materials, 2025, 8 (12), 6004,
DOI: 10.1021/acsanm.5c00144

X **Direct observation of liquid–solid two-phase seed particle-assisted kinking in GaP nanowire growth**
T. Hu, M. S. Seifner, M. Snellman, D. Jacobsson, **M. Sedrpooshan**, P. Ternero, M. E. Messing, K. A. Dick
Small Structures Journal, 2023, 4(9), 2300011,
DOI: 10.1002/sstr.202300011

Abbreviations

1D – one dimensional

DMA – differential mobility analyzer

ESP – electrostatic precipitator

SEM – scanning electron microscopy

STEM – scanning transmission electron microscopy

STXM – scanning transmission X-ray microscopy

TEM – transmission electron microscopy

XEDS – X-ray energy dispersive spectroscopy

XMCD – X-ray magnetic circular dichroism

Acknowledgements

First and foremost, I would like to express my heartfelt gratitude to **Rasmus**, my main supervisor. I truly appreciate the guidance, trust, and freedom you provided me to explore various ideas. I am especially grateful for your constructive feedback and your impressive way of articulating scientific work. Also, I would like to express my deepest gratitude to my co-supervisor, **Maria**. I truly appreciate the exceptional research environment you have fostered, as well as your continuous support and encouragement. I am grateful for all the opportunities you provided, which allowed me to evolve as a scientist and as a person. I am also deeply grateful to **Adam**, my second co-supervisor, for his invaluable support during this work. I have learned so much from you, and our discussions continuously added new dimensions to the projects.

When I first came to Lund in 2020, **Claudiu** was the one who showed me around and helped me get started with everything. Later, he also supported us with the X-ray microscopy measurements at Max IV. I am deeply grateful to you, Claudiu, for your invaluable contributions and for everything I have learned from you. I am deeply indebted to **Calle**, who was the first to teach me how to work in the spark ablation lab and who, little by little, guided me toward the topic. Your way of approaching science in a detailed and careful way has always been inspiring for me. I feel incredibly privileged to have been part of the aerosol group during this period. This group has been a place of both intellectual growth and lasting friendships. I was fortunate to get to know **Knut**, **Thomas**, **Sara**, **Linnéa**, **Markus**, and **Martin**. I have learned from each and every one of you. Thank you for all the interesting discussions and fun get-togethers at Maria's and Knut's places. A special thanks to **Bengt** for building the aerosol generator and for his deep knowledge and kind support, which made this work possible. I am grateful to **Pau** and **Marie**, with whom I shared my PhD journey from the harsh COVID-19 period to the present. I have learned so much from both of you. **Sam**, it has been a pleasure getting to know you and working with you. Your passion for research is truly admirable, and I wish you all the best in your future endeavors. A special wish for **Hajar**, who is carrying the torch forward, I hope you navigate the challenges ahead with resilience and success.

I extend my appreciation to all my colleagues at the Division of Synchrotron Radiation Research (SLjus) and the Division of Solid State Physics (FTF), as I had the opportunity to work across both divisions. I am grateful to **Vidar**, my office mate, and **Nils**, sitting in the opposite office, for the occasional chats and their amazing know-how in everything. I am thankful to **Elizabeth Blackburn** and her team members for the meetings and journal clubs related to magnetism. I would also like to thank the NanoLund technical and administrative staff for creating a stimulating research environment and providing essential support throughout this work.

A special acknowledgment goes to **Thomas Greber**, who generously welcomed us into his lab at the University of Zurich. I also sincerely thank **Davide Peddis** and **Pierfrancesco**

Maltoni, along with their group members, for their expertise and willingness to collaborate, which helped overcome the challenges posed by equipment limitations. Additionally, I am grateful to **Thomas Jespersen** and **Damon Carrad** for their warm collaboration on the electrical measurements at the Technical University of Denmark.
I am honored to have been part of the **GenerationNano** program, European Union's H2020 MSCA (Grant No. 945378), and I sincerely appreciate the coordination and support from **Gerda Rentschler**. Through this program, I have had the pleasure of getting to know **Radhika**, **Rohit**, and many others who have offered me the warmest support.
I was fortunate to do a secondment at Alfa Laval, and I would like to thank **Axel Knutsson**, **Mehdi Roozban**, **Mareddy Reddy**, and **Jenny Rehn Velut** for their openness and kind support. A special thanks as well to **Anders Mikkelsen** for making this opportunity possible.
On a personal note, I am grateful to have found amazing new friends who have been a constant source of joy and encouragement throughout this journey. **Asieh**, **Ata**, **Esra**, **Iosif**, **Mado**, **Mahsa**, **Mohammad**, **Rezvan**, **Reza**, **Shokoufa**, **Zahra**, thank you for all the fun, laughter, and unforgettable moments.
Finally, my deepest gratitude goes to my family, and especially to **Elham**, the love of my life, whose endless patience and support have been my constant source of strength.

Popular summary in English

In materials science, the most fascinating discoveries often emerge at the tiniest scales, revealing a hidden world where materials exhibit astonishing and unexpected behaviors. At those scales, tiny pieces of materials, called nanoparticles, possess unique properties that do not exist in their larger bulk forms. From enhanced strength and unexpected electrical properties to fascinating magnetic behaviors, nanoparticles are reshaping our understanding of what materials can do and opening up incredible possibilities in fields like medicine, energy, and electronics. Magnetic nanoparticles, in particular, drive innovations in healthcare, environmental remediation, energy and sustainability, and data storage solutions. Imagine a world where we can carefully select these remarkable particles and arrange them precisely next to one another, creating components that possess the unique nanoparticle properties and more extraordinary features that arise when these particles come together and interact. This concept is called nanoparticle assembly and forms the basis of the following thesis.
Anyone who has ever played with magnets knows that they have a way of arranging themselves in neat lines or patterns. It is almost like they have their own magnetic instinct, pulling together in specific ways. This is also the case for tiny magnetic particles. They have their own way of arranging. However, to build components that match our applications and needs, we need to introduce something like a permanent magnet to control the way the particles assemble. Bringing a magnet close to the tiny particles forces them to align in a straight line, much like how a magnet arranges paper clips into a chain when placed nearby. This is the effect of the magnetic field surrounding the magnet and has already been explored in good detail. However, merely using a magnet to arrange particles does not always result in components that fulfill our requirements. At times, we require greater control over the length of these chains, other times, the distance between parallel structures matters, and occasionally, we need the ability to selectively choose the elements within the particle chains. To make this happen, this work adds electric charges to the particles to increase the level of control on the particle assembly, enabling the use of electric fields in addition to the magnetic field during the assembly process.
Making magnetic particles charged is challenging. One challenge is that the particles might release their charge to the surrounding environment. Due to this, we need to keep them away from direct contact with other materials until they are settled down in desired structures. We address this challenge by employing gas-phase particle production methods as opposed to the majority of the previous works relying on solution-based synthesis. In gas-phase methods, generated particles are initially suspended in an inert gas until deposited on suitable surfaces. For producing such particles in this work, a method called spark ablation is used. This technique can produce nanoparticles from repetitive sparks between feedstock electrodes and is among the most sustainable methods for generating elemental and alloy nanoparticles, as it directly creates them from bulk materials without relying on any hazardous chemicals. Apart from enabling the charging of particles while they are suspended in

the gas, this technique offers good control of the elemental composition of particles, which allows tuning the properties of single particles simply by using the right electrode materials. Moreover, having the particles suspended in the gas provides another capability, which is the direct integration of these particles on any surface for various applications. This capability is incredibly valuable, as it allows us to, for example, arrange the particles using our electric and magnetic knobs on electronic chips for fabricating novel electric devices or even deposit them onto a flexible polymer, making the polymer magnetic and capable of being steered by magnetic fields from a distance which has significant potential for applications. The possibilities with the presented particle generation and assembly method are vast. However, to proceed further, we need to know what these structures have to show us. This work also explores the magnetic properties of these structures from both a macroscopic and nanoscopic perspective, using some of the most sensitive devices and microscopes available. Additionally, electrical devices are made out of the structures to look into the electrical signal and learn about the properties and potential use of the structures. The assembled nanoparticles are also directly incorporated into polymer films, and the polymer response to magnetic fields is examined, opening the way for the use of the structures in future applications and advancements. The results show that, first of all, the new methodology improves the control on the self-assembly process. This enables facile control over the length, separation, and composition of the structures deposited on a surface. Magnetic measurements show that the arrangement of particles into chains enhances the magnetic properties, in the sense that they are more stable in their magnetic characteristics against external magnetic fields. The direct integration of the structures for developing nanoscale devices demonstrates that the devices can be used to understand the underlying processes going on at those scales, and also shows that the devices can be developed further as low-cost sensing components. Magnetic polymers fabricated by the direct deposition of particles on flexible substrates show considerable response of the films to magnetic fields, stemming from the magnetic interactions between particles. In addition to the high response of the films, the methodology allows for the scalable production of these components, which is hard to achieve using previous methods.

Chapter 1

Introduction

Materials have always been at the heart of technological advances, defining the boundaries of what is possible. Nanotechnology has emerged as a particularly exciting area of research, allowing scientists to manipulate materials at the atomic level. By working at these incredibly small scales, it is possible to achieve properties and behaviors that differ dramatically from those of bulk materials. This ability to control matter at the nanoscale has paved the way for breakthroughs in fields like electronics and energy. Any structure where at least one of its dimensions falls into the 1-100 nm range is called a nanostructure. Nanostructures have a variety of shapes, such as nanoparticles, where all three dimensions are in the 1-100 nm range, nanochains and nanowires with two dimensions, and thin films with one dimension in this range (depicted in Figure 1.1).

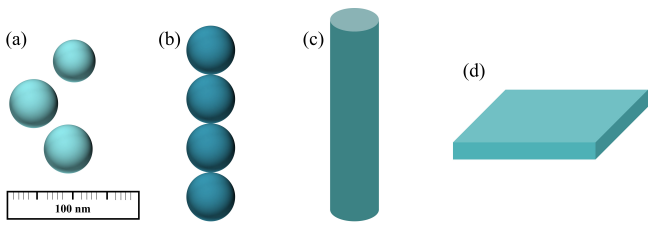

Figure 1.1: (a) Nanoparticles, (b) nanochain, (c) cylindrical nanowire, and (d) thin film.

Magnetic materials are essential for several applications, such as data storage, sensing, energy conversion, communications, and biomedicine. Within this field, magnetic nanostructures play a crucial role, as they manifest unique properties holding significant potential for developing novel applications. As an example, magnetic nanoparticles represent a fascinating class of magnetic materials with diverse applications and potentials. Since the size of the particles is comparable to the characteristic magnetic length scales, unique

magnetic features such as the single domain state and coherent magnetization switching emerge. Due to this, magnetic nanoparticles have gathered attention in storage and sensing devices as well as in biomedical engineering, where magnetic particles can be utilized for targeted therapy and as contrast agents for magnetic resonance imaging (MRI)[1, 2, 3]. Additionally, the nanoscale size of the particles provides a high surface-to-volume ratio and an enhanced number of active surface sites. This feature, together with the feasibility of steering magnetic particles with a magnetic field, has provided a capability for environmental remediation such as contaminant removal from water or soil[4, 5]. Another example is nanometer-thick multilayers exhibiting the giant magnetoresistance (GMR) effect, which revolutionized data storage technology when developed as hard disk drive read heads. This breakthrough gave rise to the field of spintronics that utilizes both the charge and spin state of the electron and holds promise for future technological developments[6].

Magnetic 1D nanostructures with high aspect ratio and anisotropic properties, such as cylindrical nanowires, have gathered significant interest, not only because of the promise of new physical phenomena[7] but also due to their great potential in magnetic storage and logic devices[8, 9, 10], spintronic applications[11, 12, 13, 14], and novel permanent magnets[15, 16]. The linear 1D arrangement of self-assembled nanoparticles, known as nanochains, forms another important class of 1D nanostructures. Nanochains have structural similarities to nanowires in that they possess a large aspect ratio and have potential applications in micro and nano actuators[17, 18, 19, 20, 21, 22, 23, 24], microwave absorption[25, 26], catalysis[27, 28], plasmonics[29, 30], sensing[31, 32], bio-medicine[33, 34], and magnetic resonance imaging[35].

Over time, different synthesis methods are developed for fabricating 1D nanostructures[36, 37]. Magnetic nanowires are typically fabricated using template-assisted electrochemical deposition, a highly versatile method that allows precise control over size, geometry, and composition[38, 39, 40]. However, this approach requires dissolving the templates and additional transfer steps to deposit the nanowires onto substrates for characterization or device integration. Alternatively, direct-write fabrication of magnetic nanostructures[41, 42], including nanowires[43, 44, 45], can be achieved via focused electron beam induced deposition (FEBID). While FEBID offers significant flexibility in the geometries it can produce, it is often limited by impurities and poor crystallinity[41, 43]. While current nanowire fabrication methods pose limitations in integrating magnetic nanostructures for practical applications, the direct self-assembly of nanoparticles holds great promise for generating one-dimensional nanostructures with high purity and desired compositions that can be easily introduced to different surfaces, to meet intended purposes[37, 46].

Most self-assembly techniques utilize nanoparticles suspended in a solution where they organize into 1D structures via interparticle interactions mediated by ligands, templates, or external fields[47, 48]. The latter approach is commonly used to form nanochains by applying a magnetic field directly to the suspension of particles or during drop-casting onto a substrate[49, 50, 51, 52, 53, 54, 55, 56]. This strategy is simple, cheap, and scalable but generally lacks precise control of the spatial distribution of the 1D structures, where chain

aggregation leads to densely packed assemblies along the surface as the solvent evaporates. Controlled positioning of nanoparticles into separated nanochains with tunable length and interchain distances has proven to be a great challenge[47], and recent progress relies on functionalizing nanoparticles[49], or top-down lithography[29, 31, 57, 58]. While these methods are suitable for certain applications, they add excessive complexity to the processes and potentially can compromise the cost efficiency and scalability that were previously regarded as the key advantages of assembly techniques. Additionally, chemical methods are primarily applicable to chemical batches and involve multiple stages to produce the final structures. This challenges the tandem production required for practical purposes.
In parallel to chemical-based methods, gas-phase (aerosol) synthesis techniques have a high potential for engineering and assembling nanoparticles[59, 60, 61]. An aerosol is a suspension of fine particles with sizes from a few nanometers to 100 µm in a gas. Aerosol synthesis methods are known for their scalability, and particles produced via these methods are of high purity and uniformity. Previous studies using aerosol methods to assemble magnetic nanoparticles have typically relied on permanent magnets for nanoparticle collection[27, 28, 62, 63]. This approach promotes particle assembly during deposition but offers limited control over the self-assembly process. Consequently, the full potential of this methodology remains unexplored. This dissertation further develops the capabilities of gas-phase nanoparticle assembly by utilizing charged magnetic particles[64] and shows how this additional degree of freedom can give rise to enhanced control on the formation of 1D nanochains and their final properties. During the self-assembly process, the nanoparticles are attracted to a substrate using an electric field, where they are self-assembled, one by one, into 1D nanochains along the direction of an applied magnetic field. Additionally, it is demonstrated that by varying the electric field, and thereby the ratio of electric and magnetic forces on particles, the spatial distribution of the deposited nanochains on substrates can be controlled. The approach is highly versatile as it relies on charged aerosolized nanoparticles, which can be produced through various methods, including atomizing particles from a chemical solution, flame spray synthesis, or evaporation techniques[65]. In this methodology, the fabrication process can be divided into particle formation and deposition. Particle formation involves the evaporation of bulk materials by physical means, particle shape modification, charging, and size selection. While the deposition involves the extraction of particles from the gas-phase using a combination of electric and magnetic fields, and the self-assembly of particles on desired surfaces. The following provides an outline of the concepts carried out in this work.

Nanoparticle Generation

As mentioned above, nanoparticles are the building blocks of the self-assembled structures. They can be formed using wet chemical methods, where the particles are synthesized from

precursors through chemical reactions. They can also be generated using gas-phase physical techniques, where they are produced through physical processes such as evaporation. The latter methodology has a much lower negative environmental impact, and the produced particles are commonly of higher purity since the process is chemical-free and does not require the introduction of impurities such as catalysts and surface modifiers.
This study uses the spark ablation method, which is a versatile and robust technique for producing gas-phase nanoparticles. This method generates nanoparticles into a carrier gas through spark discharges between two electrodes with desired compositions. Spark ablation, despite being a relatively new technique invented in the 1980s, has demonstrated highly intriguing and promising results in various fields[66]. Here, ferromagnetic nanoparticles, particularly Co (in **Paper I**, **V**, and **VI**), are generated as single-element nanoparticles. In addition to single-element nanoparticles, the spark ablation technique enables combining several different elements, including immiscible metals, into nanoparticles[59, 67]. The composition of particles has a significant effect on their physical, chemical, and optical properties and allows for tuning and optimizing the properties required for particular purposes. Therefore, the technique is also used to showcase the capability of generating alloy magnetic materials such as FeCo nanoparticles (**Paper II**) directly from the co-ablation of Fe and Co single-element electrodes and FeNi from the ablation of pre-alloyed electrodes. Additionally, in **Paper III**, the effect of reductive or oxidative carrier gases on the composition of nanoparticles produced by pre-alloyed Co-Ni electrodes is investigated.

Directed Self-Assembly of Nanoparticles

Despite the advantages of gas-phase techniques in nanoparticle production, these methods have received less attention regarding magnetic nanoparticle self-assembly. This is largely due to the greater challenges associated with collecting and assembling particles floating in a gas compared to those confined within chemical batches. In **Paper I**, the study shows that the additional degree of control, charging of particles, and combining electric and magnetic fields at the deposition stage allow for the controlled self-assembly of nanoparticles into chains, thereby expanding the capabilities of these techniques. Figure 1.2 schematically demonstrates the nanoparticle production from spark ablation to directed deposition of charged magnetic nanoparticles, together with the involved processes. In addition, **Paper I** demonstrates that once the nanochains are integrated onto the desired substrate, post-annealing can transform the structures into nanowires, overcoming the challenges associated with nanowire integration that conventional template-assisted methods face.

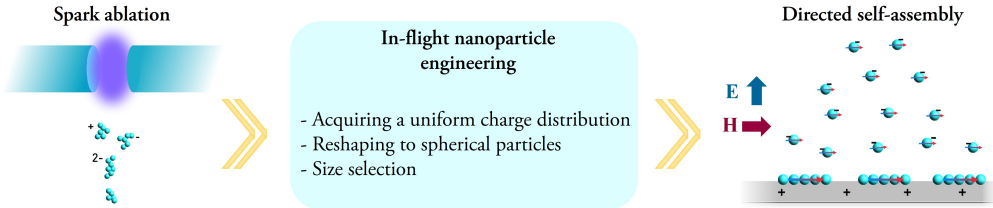

Figure 1.2: Spark ablation between two electrodes, in-flight nanoparticle engineering, and directed self-assembly of the charged magnetic nanoparticles under electric and magnetic fields.

Controlling the Composition and Spatial Distribution of Structures

As in this method, particles are gradually supplied to the substrate, as opposed to chemical-based methods that particles are introduced all at once, facile consecutive deposition of different materials on top of each other becomes possible. As shown in **Paper IV**, this enables tuning the composition of nanochains in addition to tailoring particles' composition, mentioned above. The thesis demonstrates the possibility of combining nanoparticles with different compositions, forming multisegmented chains or nanocomposite materials (shown in Figure 1.3(a)) aiming to benefit from the synergy of different material systems. Additionally, since the deposition is performed by both electric and magnetic forces, **Paper IV** shows that the interplay of the two forces applied on particles upon deposition allows for tuning the spatial distribution of structures on the surface, demonstrated in Figure 1.3(b). This is while, previously, for tuning the spatial distribution of structures, researchers have been mostly relying on low-throughput, high-cost patterning of the surface[58].

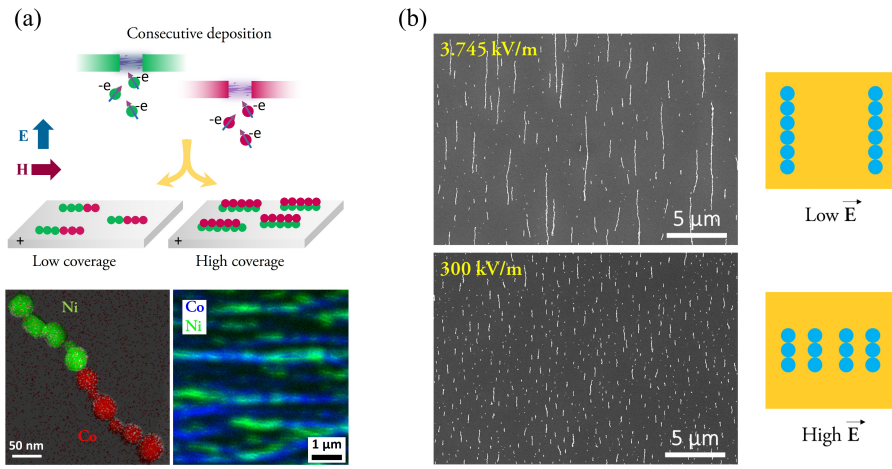

Figure 1.3: Controlling the (a) composition and (b) spatial distribution of self-assembled structures. Retrieved from **Paper IV**.

Direct Integration and Applications

A significant advantage of the methodology further developed in this thesis is the direct integration of the structures onto selected substrates. This capability can pave the way for several nanoparticle-based devices and applications. **Paper V** demonstrates that the direct assembly of particles onto flexible polymer layers allows for the facile production of magneto-responsive soft films with high magnetic response suitable for applications based on magnetic actuation. Also, **Paper VI** shows that the direct deposition of nanoparticles onto pre-patterned Si chips allows for the fabrication of electrical components consisting of nanoparticle assemblies, which in this work are used to analyze the magnetization reversal through the magnetoresistance signal. These components hold potential for low-cost sensing applications. Figure 1.4 schematically shows the direct integration of nanoparticles in this thesis, for producing microscale magnetic soft films and nanoscale devices.

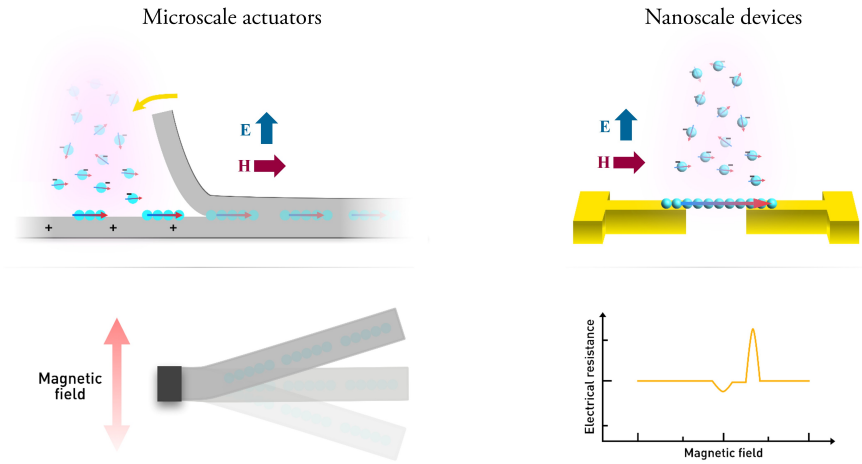

Figure 1.4: Direct integration and self-assembly of nanoparticles for the fabrication of microscale soft films and nanoscale devices.

Investigating the Magnetic Properties

This thesis places significant emphasis on the detailed magnetic characterization of most of the systems produced in this work. It examines nanoparticle assemblies from both an ensemble-averaged perspective (in **Paper I**, **II**, and **V**), using magnetization curves obtained through various protocols, and a nanoscopic perspective (in **Paper I**, **II**, and **VI**), employing X-ray microscopy and magnetoresistance measurements on individual structures. In addition to the experimental studies, micromagnetic simulations are developed on systems closely matching the experimentally produced structures to look into the details of mag-

netization reversal in nanochains. Figure 1.5 shows an overview of magnetic studies carried out on the self-assembled structures.

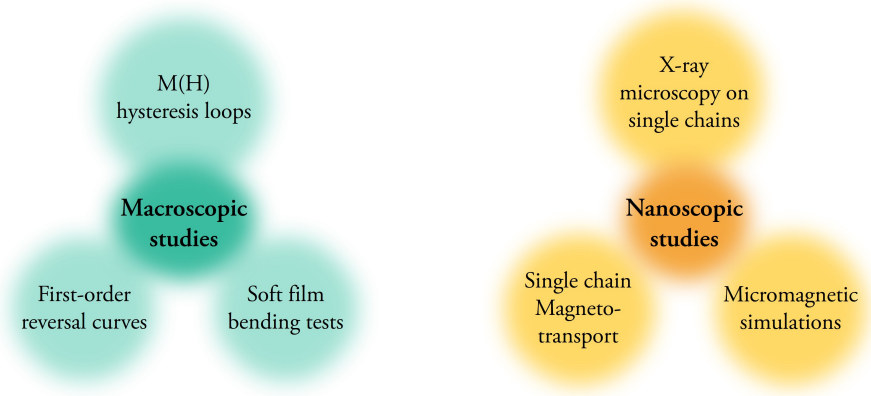

Figure 1.5: Nanoscopic and macroscopic studies carried out on the structures.

Scope of the Thesis

In Chapter 2, the dissertation starts by focusing on the nanoparticle generation in the gas phase using the spark ablation method and then the self-assembly process. The chapter continues on the possibilities of tuning the composition and morphology of structures. Also, by demonstrating the capability of the methodology on the direct integration of structures, the promise of the method in practical applications is shown. Chapter 3 gives an overview of the fundamentals of magnetism in the structures. Chapter 4 elaborates on the employed experimental means and the developed micromagnetic simulations. Finally, Chapter 5 presents the main conclusions and outlook.

Chapter 2

Magnetic Nanoparticles; Generation, Self-Assembly, and Processing

2.1 Spark Ablation and Nanoparticle Generation

The spark ablation technique is a versatile method for generating nanoparticles in the gas phase. It offers a large selection of building blocks, ranging from single-element[64] and alloy[68, 69, 70, 71] nanoparticles to bi-magnetic systems[72, 73]. This technique has recently become commercialized, indicating its outstanding performance and potential in various materials research and production areas. A detailed description of the method is provided in Ref[66].

As shown in Figure 2.1, nanoparticle generation starts from the evaporation of materials by repetitive sparks between two conducting rods composed of the materials of interest under a carrier gas flow. The pressure in the system is kept constant during the generation process at around 1015 mbar. As the evaporated material in a supersaturation state cools down, it condenses into atomic clusters and then typically sub-10 nm primary particles that collide, forming larger irregular agglomerates, which are then passed through a Ni^{63} diffusion charger to obtain an even charge distribution. This balance in the charge distribution is needed for the size selection of the produced nanoparticles. The agglomerates are then transported through a tube furnace, where they are compacted into single-crystalline nanoparticles before being size-selected based on their electrical mobility diameter using a differential mobility analyzer (DMA). The particle concentration can be monitored online with an electrometer (EM), and subsequently, the deposition time to obtain the desired coverage can be calculated based on Ref[74]. A description of the bipolar diffusion charger, DMA, EM, and electrostatic precipitator (ESP) is provided in the Appendix.

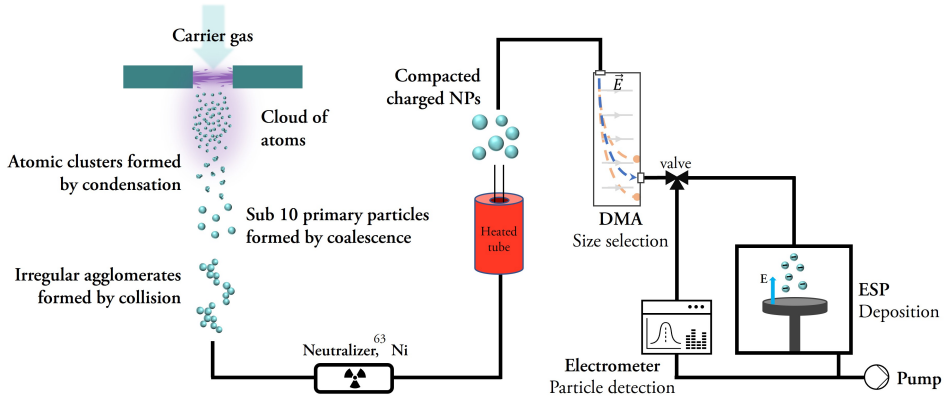

Figure 2.1: A schematic of the spark discharge generator (SDG) system used in this work.

2.2 Self-Assembly of Magnetic Nanoparticles

The collection of magnetic nanoparticles on a substrate is conducted in the ESP chamber, shown in Figure 2.1. ESP provides an electric field up to a few hundred kV/m, which attracts negatively charged particles to the substrate. To assemble the magnetic particles in parallel nanochains, a magnetic field is applied to the substrate, by placing it on a permanent magnet as shown in Figure 2.2(a). Figure 2.2(b) schematically shows the assembly process. As the charged magnetic particles approach the surface, they are subjected to four main forces mediated by the electric field, magnetic field, magnetic dipolar interactions, and Brownian motion. This can be described as

$$m_p \frac{dv_p}{dt} = F_{ESP} + F_{\Delta H} + F_{dipolar} + F_B, \tag{2.1}$$

where F_{ESP} consists of all forces, such as Coulomb, image, and van der Waals forces, associated with depositing charged nanoparticles onto a flat surface using an electric field[75]. $F_{\Delta H}$ is the magnetic force from a magnetic field gradient, $F_{dipolar}$ is the magnetic dipole-dipole forces between incoming and deposited nanoparticles, and F_B is the force due to the Brownian motion of nanoparticles. A detailed modeling of the self-assembly process is presented before in Ref[64, 76].

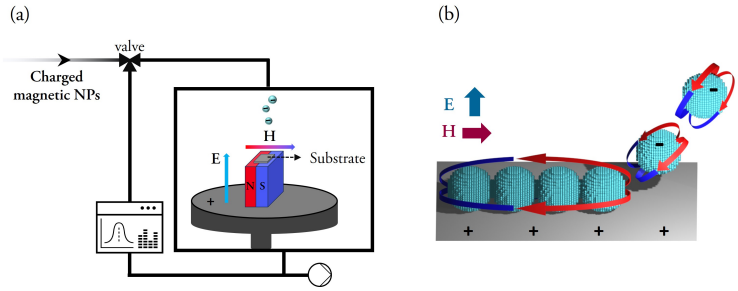

Figure 2.2: (a) Deposition chamber with the permanent magnet underneath the substrate. (b) Schematic of the directed self-assembly of gas-phase magnetic nanoparticles under electric and magnetic fields.

Ferromagnetic nanoparticles are spontaneously magnetized and self-assemble into 3D interconnected chains due to the random magnetization direction of the incoming and deposited particles. In contrast, applying an external magnetic field aligns the particle magnetic moments, and the self-assembly results in the formation of 1D chains of particles along the direction of the magnetic field. Figure 2.3(a) shows identical-location electron microscopy images of a single FeCo nanochain being assembled over time as particles are added one by one. Moreover, Figure 2.3(b) illustrates that in regions of the sample where incoming particles are attracted to the top of the structures, the formation of parallel chains or bundles occurs. The arrows in the image highlight particles deposited on top of the structure, nucleating bundle formation. The length of the structures can be controlled by the number of deposited nanoparticles or, in fact, the deposition time. Figure 2.3(c) displays the correlation between the average length of FeCo nanochains and the deposited number of particles per surface area. The linear relation between the two parameters enables straightforward control over the nanochain length.

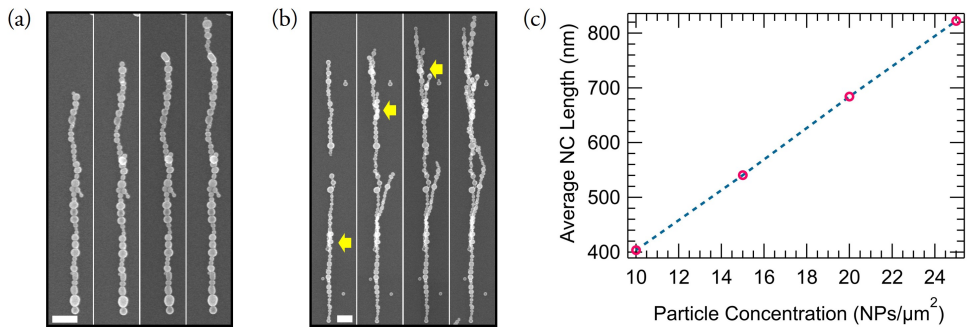

Figure 2.3: (a) Identical-location electron microscopy image of a single nanochain displaying the nanochain formation. (b) Nucleation of parallel chain formation (bundles) from particles deposited on top of chains (scale bars = 200 nm). (c) The average length of FeCo nanochains per deposited particle concentration. Retrieved from **Paper II**.

2.2.1 Tuning the Spatial Positioning of Incoming Particles

The spatial distribution of nanochains on the surface determines interchain interactions and the resulting magnetic characteristics of the system. One important finding of this work is that the spatial distribution of chains can be tuned by varying the forces applied on the particles, presented in **Paper V**. As particles get close to the substrate, there are two main forces that attract them to the surface, electric force from the ESP and dipolar magnetic forces between the particles. The former attracts the nanoparticles uniformly to the substrate surface, whereas the latter is between the already deposited and arriving nanoparticles, which leads to the anisotropic self-assembly. Thus, the interplay between the two forces determines if the nanoparticles are preferentially attracted to the substrate or the nanoparticles. The latter leads to longer chains with larger separation, while the former leads to a more uniform distribution of the particles with shorter inter-particle separation and, thus, shorter chains. Figure 2.4(a) and (b) show SEM images and image analysis of nanochains formed under different electric fields. The particle coverage in these images are approximately the same, however, they are arranged in different ways depending on the electric field strength. It is observed that lower electric fields (below $\approx$ 75 kV/m) give rise to the formation of longer chains, meaning that the incoming particles are more effectively attracted to the already deposited structures. In addition, at low electric fields, nanochains tend to grow with larger separations in between. This occurs because the magnetic dipolar force in Equation 2.1 dominates by diminishing the influence of the electric force. For instance, the magnetic dipole-dipole force between two 40 nm cobalt nanoparticles separated by 500 nm is in the order of 10^{-12} N. In comparison, the force exerted by a uniform electric field on a singly charged nanoparticle decreases from 10^{-13} to 10^{-16} N as the field strength is lowered from 750 to 3.75 kV/m. This interplay between magnetic and electric forces enables tuning the nanoparticle assembly process and, thus, the final deposited structures by only changing the electric field during the deposition. Figure 2.4(c) schematically shows the structures formed by the same number of particles at low and high electric fields. This achievement is valuable as the process does not rely on adding complexities to the self-assembly process. Conventionally, to control the interchain distances, lithographic patterning or changing the amount of material had to be used to vary the chain separation. These methodologies either add complexity to the self-assembly process or substantially change the magnetic system.

It should be noted that, as aerosol nanoparticles tend to follow the carrier gas flow due to the drag force, there should be sufficient attractive forces applied to the particles upon deposition to effectively extract the particles from the gas phase. Thus, at low electric fields (approximately lower than 75 kV/m), where the total attractive forces applied on the gas-phase particles are reduced, the control on the deposition of particles on a well-defined area decreases. Moreover, in the absence of strong forces, the Brownian motion of the particles becomes more pronounced, resulting in a random placement or loss of particles. As a result, at low electric fields particle deposition occurs with a lower efficiency and also over a

larger area, which ultimately increases the deposition time required for reaching a desired particle concentration on the substrate. Therefore, in the case of 40 nm Co nanoparticles, a minimum electric field from 75 kV/m is preferable.

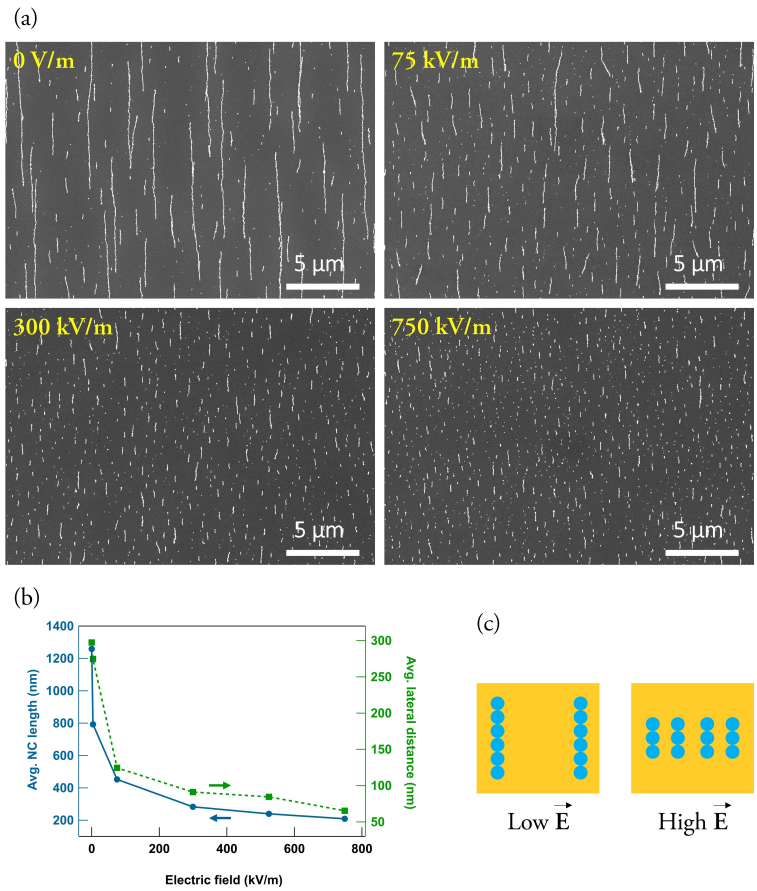

Figure 2.4: (a) Co nanoparticle self-assembly at different electric fields. (b) Average nanochain length and lateral separation per electric field. (c) A schematic showing the effect of the electric field on the final particle assembly structures, considering the same number of particles. Low $\vec{E}$ (high $\vec{E}$) refers to electric fields approximately below (above) 75 kV/m. Retrieved from **Paper IV**.

2.2.2 Tailoring the Nanochain Composition

Tailoring the composition of nanoparticles allows for tuning the physical properties of the nanochains for various purposes. The spark ablation method used here for generating aerosolized particles allows for tuning the composition by varying the electrode bulk materials and small adjustments in the production process. Mixing different elements can be achieved through various strategies, such as using different materials as the anode and

cathode or using pre-alloyed electrodes. The mixing of materials occurs upon ablating the electrodes, and material properties and thermodynamics of the involved processes determine the final state of the nanoparticle composition to be in the form of alloy, Janus, or core-shell[68, 77, 78]. **Paper II** demonstrates that the co-ablation of Fe and Co single-element electrodes leads to alloy nanoparticles with a Fe:Co ratio close to 50:50. Figure 2.5, shows a schematic of the approach together with an electron image with chemical contrast from FeCo particles showing the uniform distribution of the elements in the particles. If other elemental ratios are needed, one option is to use pre-alloyed electrodes with desired compositions[70]. Figure 2.6(a), shows an schematic of permalloy $Fe_{20}Ni_{80}$ nanoparticle formation using this approach. Figure 2.6(b) and (c) shows that the process has resulted in the formation of single-phase FeNi alloy nanoparticles with a lattice parameter of 3.551 ± 0.001 Å matching FeNi 20:80 and a shift in the X-ray diffraction (XRD) pattern compared to pure Ni[79]. These two alloying methods further enhance the capabilities of the methodology and allow for the single-step generation and assembly of 1D structures with tuned compositions.

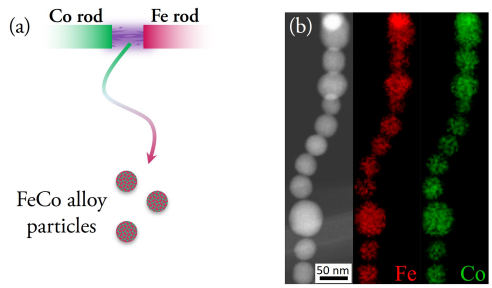

Figure 2.5: (a) Schematic of the co-ablation of Fe and Co rods for generating FeCo alloy nanoparticles, (b) electron microscopy chemical maps of the particles showing uniform distribution of elements, ≈ 50:50 Fe:Co ratio (**Paper II**).

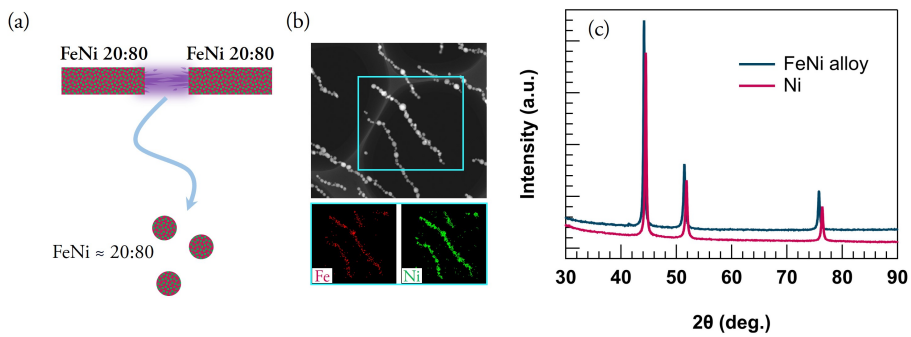

Figure 2.6: (a) Schematic of the ablation of FeNi pre-alloyed rods with 20:80 at% composition for generating specific alloy nanoparticle compositions. (b) STEM-XEDS image, and (c) XRD of FeNi particles demonstrating the formation of a single fcc-FeNi 20:80. The FeNi XRD pattern is compared to that of pure fcc-Ni nanoparticles, showing a clear shift in the lattice parameter due to the alloying.

Another strategy for tuning the composition of nanochains is assembling nanoparticles of different compositions through consecutive depositions. This approach leverages the synergy of the materials' properties to obtain improved performance, for instance, in catalysis or for engineering the magnetic properties[80]. Consecutive low-coverage deposition of nanoparticles of different compositions leads to segmented nanochains, as illustrated in Figure 2.7 in the case of Co and Ni.

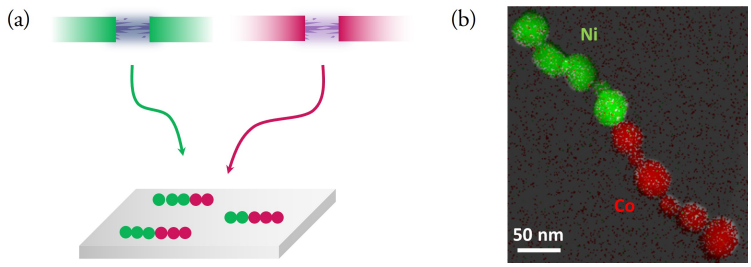

Figure 2.7: (a) Schematic illustration of multisegmented chain fabrication, and (b) STEM-XEDS image of a Co-Ni segmented structure produced by the consecutive deposition of Co and Ni particles at low coverages. Sourced from **Paper IV**.

At higher coverages, the same approach produces bundles of parallel nanochains with different compositions, see Figure 2.8. This approach increases the likelihood of interchain exchange interactions as they are laterally connected. An innovative example would be to combine magnetically hard and soft magnets with a 1D geometry to create hard/soft exchange coupled composites combining the large anisotropy and high magnetization of the hard and soft phases, respectively[81].

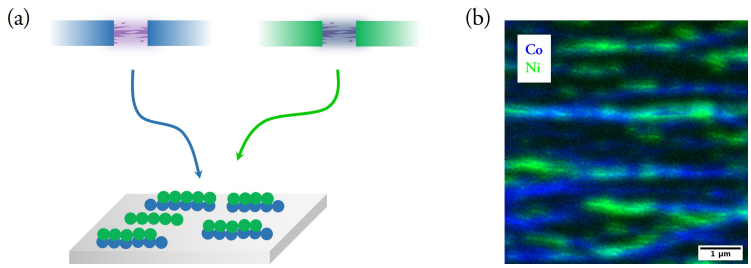

Figure 2.8: (a) Schematic illustration of nanocomposite fabrication, and (b) X-ray fluorescence microscopy image of Co-Ni parallel chains, produced by the high-coverage deposition of the particles. Retrieved from **Paper IV**.

In addition to the electrodes and consecutive depositions, another control knob for tuning the composition of nanoparticles is the carrier gas. The introduction of reductive or oxidative environments during the particle generation process can lead to the formation of metallic or oxide nanoparticles. Although in this work, most particles are generated under a reductive carrier gas (N_2 with 5% H_2) resulting in metallic nanoparticles, the influence

of carrier gases containing oxygen on the composition of particles is also explored. **Paper III** examines the change in the composition of particles produced from pre-alloyed CoNi electrodes under reducing (95% N_2 + 5% H_2), inert (N_2), and oxidative (air) environments. A schematic illustration and chemical maps of the produced particles are shown in Figure 2.9. The results demonstrate that this strategy enables the transformation of particle composition from metallic to oxide while also allowing the formation of bi-magnetic systems in partially oxidized particles.

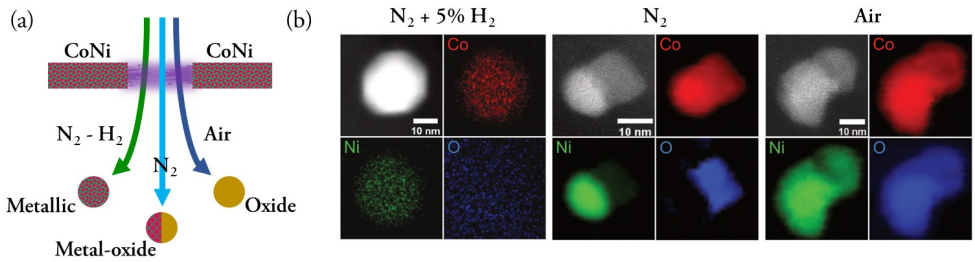

Figure 2.9: (a) Schematic illustration and (b) chemical maps of particles produced from CoNi pre-alloyed electrodes under different carrier gases. Taken from **Paper III**.

2.3 Continuous Generation and Direct Integration

As demonstrated in **Paper I**, **V**, and **VI**, a key feature of the self-assembly technique demonstrated in this thesis, is the ability to continuously generate nanoparticles and directly integrate them onto chosen substrates. This provides a versatile route to realize various nanoparticle-based components with a wide range of possibilities. The large-scale production of these components could be envisioned through the automated motion of the particle jet nozzle or substrate, which is currently being developed for fabricating porous films used in catalysis[66]. In this work, the direct integration of nanoparticles is explored mainly for two purposes: first, to develop magnetoresponsive soft films, and second, to incorporate nanochains into electrical circuits. As shown in **Paper V**, the direct integration of nanochains into polymer layers facilitates the fabrication of magneto-responsive films for magnetic actuation. The fabrication technique presented here is based on the self-assembly of the gas-phase nanoparticles into nanochains on a polymer layer and then lamination of the materials to secure the particles at the interface, Figure 2.10(a). The produced magnetic soft films have a high magnetic response to magnetic fields as shown in Figure 2.10(b), where a magnetic film composed of Co nanochains is freestanding vertically on a permanent magnet with the chain axis along the field direction. Moreover, the bending performance of samples produced on polyolefin and Kapton tapes is shown in Figure 2.11. The results show a considerable bending angle of $36 \pm 1^\circ$ at 1 T and show that the bending angle can be tuned by the amount of deposited materials and the mechanical properties of the polymer

layer.

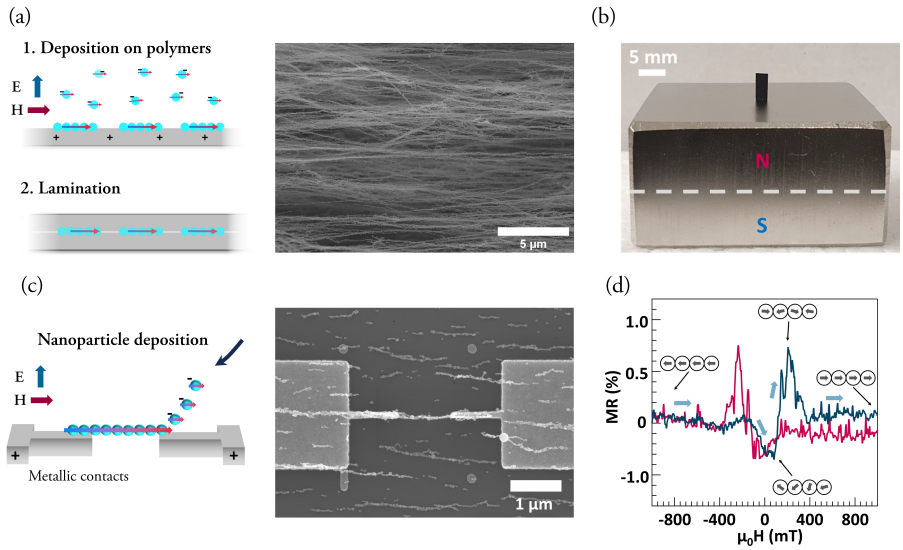

Figure 2.10: (a) Direct integration of nanochains on soft polymer layers. (b) A fabricated magnetic film freestanding vertically on a permanent magnet, while the magnetic easy axis of the film follows the field lines of the magnet. (c) nanoparticle self-assembly on metallic contacts, (d) the variation in MR response of the device correlated to different magnetic states. Reproduced from **Paper V** and **VI**.

Figure 2.10(c) illustrates a 1D assembly of nanoparticles bridging the gap between two metallic contacts, completing the two-terminal circuit. This straightforward approach, explored in **Paper VI**, allows for the facile fabrication of magnetoresistive devices with anisotropic properties and represents the first realization using single nanochains as the sensing elements. In these devices, the electric conductance and the magnetic state of nanostructures are interconnected, enabling both the study of magnetization switching and the potential development of a low-cost magnetic sensing approach. In **Paper VI**, the study of the magnetoresistance properties of these devices, as shown in Figure 2.10(d), provided information about the magnetization switching in these structures, which, to the best of our knowledge, has not been previously reported.

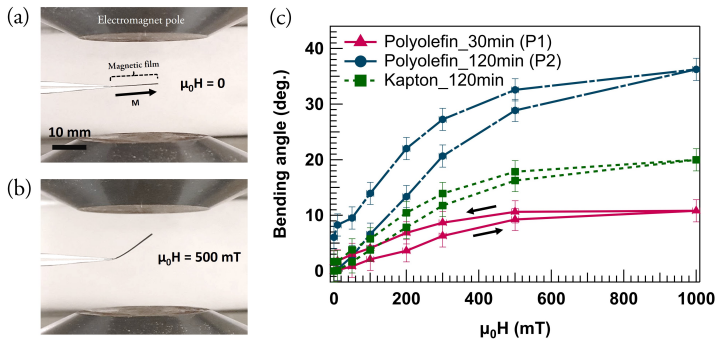

Figure 2.11: A magnetic film, labeled as P2, with 12.5×1.6 mm rectangular film between the poles of an electromagnet at (a) 0 and (b) 500 mT fields. (c) Quantitative analysis of bending angle per magnetic field for samples produced using polyolefin and Kapton tapes. Taken from **Paper V**.

2.4 Post-Processing of Assembled Structures

In addition to controlling the composition, tailoring the morphology of nanochains opens up new possibilities in tuning the magnetic properties. This work demonstrates that the morphology can be transformed from nanochains to nanowires by post-annealing. Although nanochains and nanowires share features such as magnetic shape anisotropy, they maintain distinct magnetic characteristics due to the differences in the dominant magnetic interactions within the structures, as investigated in **Paper I** and **V**.

Figure 2.12(a)-(c) displays an as-prepared and two post-annealed nanochains at 400 and 500 C for 2 min, respectively. At relatively lower annealing temperatures, the nanoparticles start to fuse to create continuous 1D structures with strong diameter modulation, whereas increasing the temperature leads to cylindrical-like nanowires. **Paper I** and **V** study the effect of post-annealing on the magnetic properties of nanochains using experimental and simulation techniques and show that transformation of nanochains to nanowires, leading to a change in the dominant interparticle interactions, from dipolar to exchange, considerably affects the magnetic properties.

Despite the significant research into the self-assembly of nanoparticles, studies of post-processing are largely absent in the literature, and post-annealing of nanochains has only been studied by theoretical models and simulations[82, 83]. Figure 2.12(d) shows a descriptive illustration of the shape change by post-annealing. In the initial phase, the chain develops a smooth surface curvature. During this step, the chain first transforms into a diameter-modulated nanowire and then into a smooth cylindrical shape. As annealing progresses, the cylindrical shape undergoes axial shrinkage, forming oval shapes to minimize the surface area. Eventually, upon continued annealing, the structures converge into spheres. However, the mechanism has a clear dependency on the length of the structures, and as the number of particles in a chain increases, more complex phenomena, such as the mass accumulation at the ends of the cylinder and fragmentation, are expected.

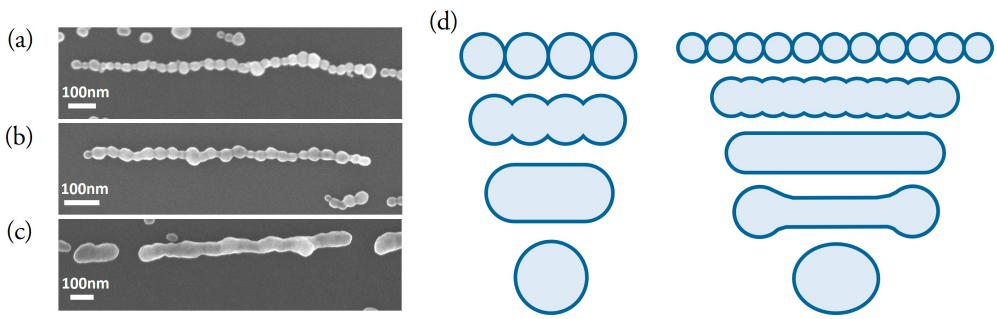

Figure 2.12: SEM image of (a) an as-prepared nanochain, (b) a diameter-modulated nanowire formed by post-annealing at 400 C, and (c) a cylindrical-like nanowire fabricated by post-annealing at 500 C for 2 min. Extracted from **Paper I**. (d) Descriptive illustration of morphology change from nanochains to diameter-modulated nanowires and nanowires, and then progression to spheres (adopted from Ref[82]).

Chapter 3

Nanomagnetism

Nanomagnetism is a field of research dealing with the magnetic properties of nanostructures and related phenomena. At these scales, materials exhibit unique behaviors governed by the material's intrinsic properties, crystal structure, size, and shape. The following chapter provides an overview of the magnetism of nanoscopic objects with a focus on nanoparticles and particle assemblies.

3.1 Fundamentals

3.1.1 Magnetic Ordering

Atoms with partially filled valence shells have a magnetic dipole moment, $\vec{m}$, due to the electrons' orbital and spin angular momenta. The atomic magnetic moment of the $3d$ elemental solids and alloys studied in this thesis are mainly determined by the spin angular momenta. The spin magnetic moment of a single electron is given by

$$m = -2\mu_B m_s,$$

where $m_s = \pm 1/2$ are the two projections of the spin angular momentum along a quantization axis, referred to as "spin-up" and "spin-down", and μ_B, Bohr magneton, is the unit of electron magnetic moment. Note that the projected spin angular momenta m_s is in the opposite direction to the resulting magnetic moment.
The vectorial sum of the atomic magnetic moments per unit volume is called magnetization, $\vec{M}$. In most elemental solids, magnetization at room temperature is zero since there is no preferred orientation of the atomic magnetic moments in the absence of an applied mag-

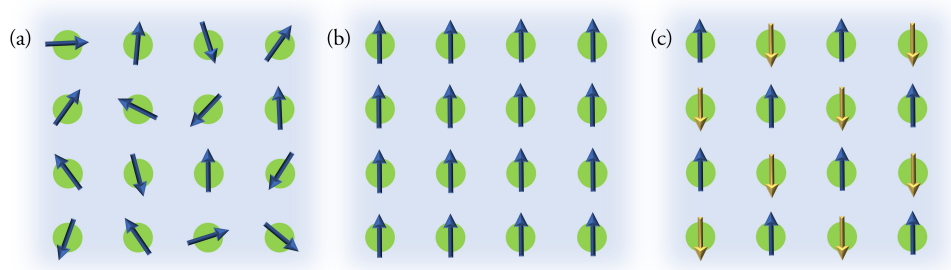

Figure 3.1: (a) Paramagnetic, (b) ferromagnetic, and (c) antiferromagnetic state. Vectors represent the magnetic moment of the atoms.

netic field. This state is called paramagnetism and is illustrated in Figure 3.1(a). However, for Co, Ni, and Fe, the alignment of magnetic moments, called spontaneous magnetization, leads to a permanently magnetized state. The origin of spontaneous magnetization is the exchange interaction between the atomic spins. The exchange interaction between two electrons sitting on neighboring atoms can be described by the Heisenberg Hamiltonian

$$H = -2\mathcal{J}\hat{\mathbf{S}}_1 \cdot \hat{\mathbf{S}}_2, \tag{3.1}$$

where $\hat{\mathbf{S}}_1$, and $\hat{\mathbf{S}}_2$ are dimensionless spin operators, and $\mathcal{J}$, is the exchange constant defining the nature and strength of the interaction. For $\mathcal{J} > 0$, a ferromagnetic ordering with parallel spins is favored, whereas an antiparallel spin configuration, called antiferromagnetic ordering, occurs for $\mathcal{J} < 0$, Figure 3.1. The strength of the exchange constant defines the temperature up to which the magnetic order is retained, which in ferromagnetic materials is known as the Curie temperature.

The magnetic moments of the transition metal ferromagnets are almost entirely due to the $3d$ valence electrons. In a solid, the atomic valence states form energy bands. For a ferromagnet, the density of states for the $3d$ band can be divided into "spin-up" and "spin-down," which are separated in energy by the exchange interaction, Figure 3.2. The exchange splitting leads to a difference in electron population, where the states with lower energy are referred to as the "majority band," and the states of higher energy are called the "minority band." The imbalance between the "majority spin" and "minority spin" leads to a net magnetization. As will be discussed in the following sections, this imbalance in the electronic states plays a key role in electrical transport in magnetic materials, as well as their interactions with X-rays.

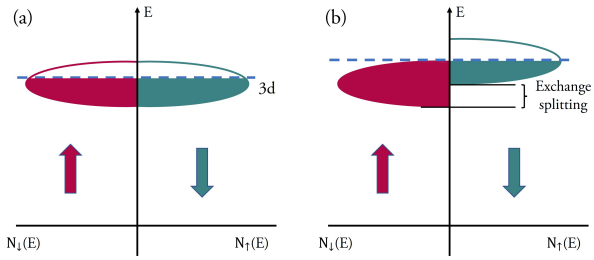

Figure 3.2: Schematics of 3*d* band structure (a) without and (b) with the exchange interaction. N(E) shows the density of states with spin-up and spin-down electrons, and the colored arrows represent the magnetic moments in the two sub-bands, which are antiparallel to the spin directions "up" and "down."

3.1.2 Magnetic Anisotropy

The exchange interaction described by Equation 3.1 is isotropic and does not favor the alignment of the atomic magnetic moments in specific directions. Magnetic anisotropy refers to energetically favorable directions for the magnetization called the easy axis/plane, while those where the energy is maximized are referred to as the hard axis/plane.The easy axes can form for several reasons, including the crystal structure and shape of the system. The anisotropy that stems from the crystal structure is called magnetocrystalline anisotropy (MCA). The MCA arises from electrostatic interaction between the anisotropic charge distributions associated with the electron's orbital angular momentum and the neighboring ionic charges, referred to as crystal fields. Depending on the crystal field and valence states, specific energetically favorable crystallographic directions (easy axis) exist, to which the isotropic spin magnetic moment couples through spin-orbit interaction. A first order approximation of the MCA energy density of hexagonal and cubic crystals can be expressed as

$$E_{MCA}^{hex} = K_1 sin^2\theta,$$
$$E_{MCA}^{cubic} = K_1(\alpha_1^2\alpha_2^2 + \alpha_2^2\alpha_3^2 + \alpha_3^2\alpha_1^2)$$

where θ is the angle between the magnetic moment and the easy axis, K_1[J m^{-3}] is the anisotropy constant, and α_i are the direction cosines of magnetization. As seen in Figure 3.3 and the expression above, hexagonal crystals have a uniaxial anisotropy with an easy axis and a perpendicular hard plane. Crystals with cubic MCA have easy axes along the <100> or <111> directions depending on if $K_1 > 0$ or $K_1 < 0$. Examples of hexagonal and cubic crystals are Co-hcp and Co-fcc.

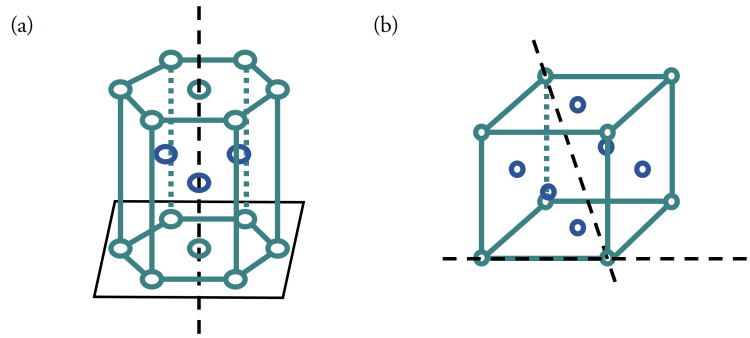

Figure 3.3: MCA easy axes in (a) hexagonal and (b) cubic crystal. In the latter, the easy axes are along the <100> or <111> directions, depending on whether $K_1 > 0$ or $K_1 < 0$.

Another important type of magnetic anisotropy in this work originates from the shape of the nanostructures. The magnetization generates a magnetic field inside the material, referred to as the demagnetization field. For anisotropic shapes, the magnetostatic interaction between the magnetization and the demagnetization field is minimized along specific directions, resulting in a so-called shape anisotropy. The magnetostatic energy density of an ellipsoid can be written as

$$E_{MS} = -\frac{1}{2}\mu_0 \vec{H}_d \cdot \vec{M} = \frac{1}{2}\mu_0 N_d M^2, \tag{3.2}$$

where M is the magnetization, H_d the demagnetization field, and N_d the demagnetizing factor along a specific direction. For a spherical object, the demagnetization factor N_d is $1/3$ in all directions. In an infinitely long cylindrical nanowire, N_d is 0 along the wire axis and 1 in the perpendicular direction. Similarly, for an infinitely thin film, N_d is 0 for in-plane magnetization and 1 for out-of-plane magnetization. Figure 3.4, illustrates the easy and hard axis for these shapes.

In nanochains, the magnetization tends to lie along the long axis, similar to nanowires. However, in nanochains, this is the magnetostatic coupling between the magnetization of the nanoparticles that leads to a uniaxial anisotropy along the 1D assembly. Therefore, this anisotropy is often interchangeably referred to as shape anisotropy or interaction anisotropy.

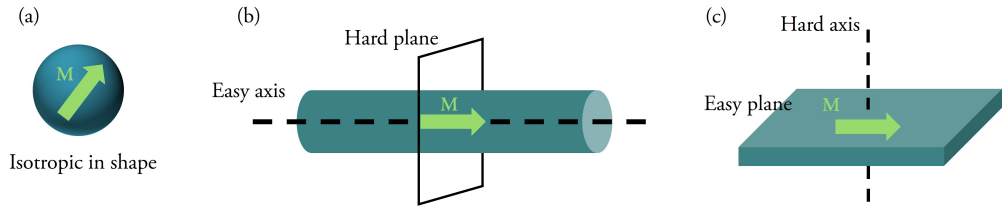

Figure 3.4: Examples of easy and hard axes/planes based on the shape of nanostructures (a) isotropic nanoparticles, (b) nanowires with uniaxial shape anisotropy, and (c) thin films with an easy plane.

3.2 Domain Formation in Nanostructures

As the Hamiltonian in Equation 3.1 depends on the scalar product of the spins, the exchange energy (with $\mathcal{J} > 0$) favors a parallel ferromagnetic ordering of the atomic magnetic moments within structures. Having all the moments aligned throughout the whole volume leads to a so-called single domain state (Figure 3.5) in sufficiently small nanoparticles. As mentioned above, the interaction between the particle's magnetization and the demagnetizing field is unfavorable as they are antiparallel, see Equation 3.2 and Figure 3.5(a). The magnetostatic energy increases with particle size as the magnetization and the resulting demagnetization field become larger. Due to the unfavorable increase in the system's energy, the magnetic material splits into domains when the particle size reaches a critical value known as the single-domain diameter to minimize the magnetic energy. Figure 3.5(b),(c) schematically illustrate the minimization of the demagnetization field by domain formation.

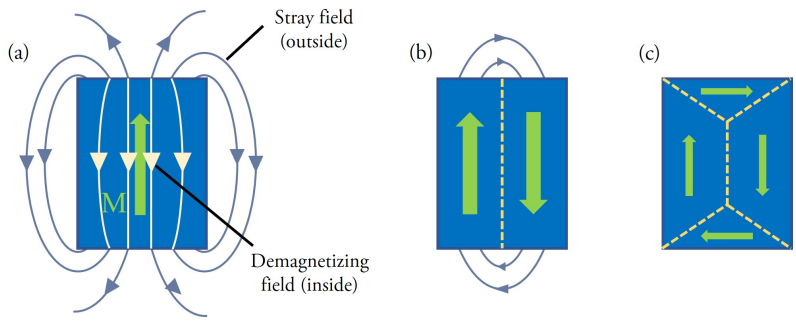

Figure 3.5: (a) Single domain state and (b),(c) forming multi-domain state to minimize the magnetostatic energy.

When magnetic domains form, the magnetization at the domain boundaries undergoes a gradual transition between the two directions. This occurs because a sudden flip in magnetization from one atomic plane to the next in ferromagnets significantly increases the exchange energy. As a result, in these regions, known as domain walls, the magnetiza-

tion gradually reorients from one direction to another along a characteristic width given by $\delta_\omega = \sqrt{\frac{A}{K_1}}$ typically ranging from 10 to 100 nm in most materials. Here K_1 is the anisotropy constant, and A is the exchange stiffness, which is proportional to the exchange constant by $A \propto \mathcal{J}S^2 Z_c/a$ where S is the spin quantum number of the material, Z_c is the number of atoms per unit cell, and a is the lattice parameter. The formation of domain walls increases the exchange energy as reorientation creates an angle between magnetic moments. Thus, one can conclude that the possibility of domain formation is subject to the interplay between the magnetostatic, exchange, and anisotropy energies. Based on this, the critical diameter is proportional to the following relation

$$D_c \propto \frac{\sqrt{AK_1}}{\mu_0 M_s^2},$$

where A and K_1 are the exchange stiffness and anisotropy constant as before, and M_s is the saturation magnetization, *i.e.*, the maximum magnetization when all magnetic moments are fully aligned[84]. When assembling these particles into nanochains, the magnetic configuration depends on the interparticle interactions, chain morphology, and the crystallographic orientation of the individual nanoparticles. In such cases, magnetic simulations, such as micromagnetics, can incorporate the aforementioned energy contributions and the morphology to determine the magnetic configurations. These simulations provide valuable insights into the magnetic behavior of nanostructures and their preferred magnetization states. Figure 3.6(a) and (b) present the simulation results of the magnetization state in nanochains after removing a saturating transverse magnetic field, considering cases where the MCA of particles are either randomly oriented or aligned along the chain axis. The results suggest that when the shape anisotropy and MCA of nanoparticles are aligned, the chains acquire a single domain state with moments along the chain axis. However, when the MCA of nanoparticles is randomly oriented, the formation of antiparallel domains along the chain occurs. Furthermore, Figures 3.6(c) and (d) illustrate the incorporation of a multi-domain particle into the chains for both randomly oriented and aligned MCA systems. The results show that, in the case of randomly oriented MCA, the antiparallel domains share a domain wall in the large particle. In contrast, the aligned MCA system forms a vortex-like structure within the large particle. Further analysis of domain formation under zero magnetic field is studied in **Paper I**.

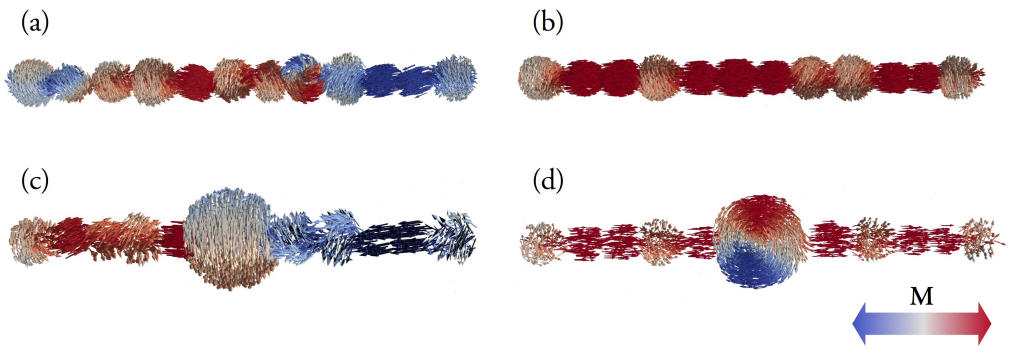

Figure 3.6: Simulated magnetization state of Co-fcc nanochains without and with the inclusion of a multi-domain nanoparticle after removing a saturating transverse applied magnetic field. Nanochain with (a) random MCA, and (b) aligned MCA. Nanochain with the inclusion of a multi-domain particle with (c) random MCA, and (d) aligned MCA. Taken from **Paper I**.

3.3 Magnetization Reversal in Nanostructures

The previous sections have focused on the equilibrium magnetic configuration in the absence of an applied magnetic field. However, understanding and controlling the magnetization reversal and domain propagation are crucial for most applications. The following section will describe these processes in single nanoparticles and nanochains. When an external magnetic field $\vec{H}$ is applied to a magnetic material, the system energetically favors aligning the magnetization with the field based on the Zeeman energy density,

$$E_Z = -\mu_0 \vec{M} \cdot \vec{H},$$

with μ_0 being the vacuum magnetic permeability. By varying the field while investigating the magnetization, valuable information about the magnetic system can be achieved. One main method is acquiring a magnetization curve of materials, where the magnetization value is plotted as a function of the applied field from a saturation state to a reversed saturating field. This measurement determines the sample's saturation magnetization, M_s, remanent magnetization, M_r, and coercivity, H_c, depicted for a ferromagnetic material in Figure 3.7(a). The remanent magnetization shows the remaining magnetization of the specimen when removing the external field, and coercivity determines the reversed field in which the net magnetization becomes zero.
Depending on the size of magnetic structures and also the exchange and anisotropy energies of material systems, the M_s, M_r, H_c vary. Magnetic materials can generally be categorized into hard, soft, and intermediate types. In hard magnetic materials, the resistance against demagnetization is high, and thus these materials possess large H_c values (Figure 3.7(a)). On the other hand, in soft magnetic materials, the tendency to demagnetization through spin

reorientation is high, and these materials have small coercivity values, although commonly having relatively high saturation magnetization (Figure 3.7(b)). Finally, the intermediate type falls between these two categories.

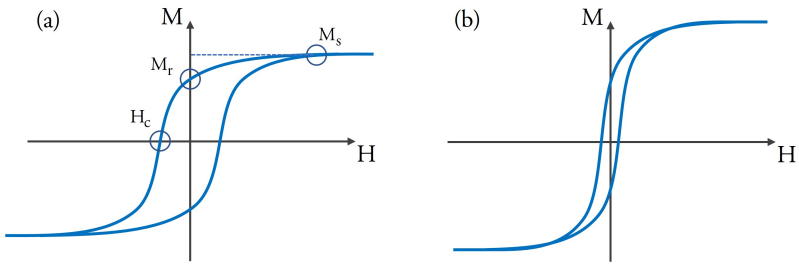

Figure 3.7: Magnetic hysteresis loop with highlighted saturation magnetization, M_s, remanent magnetization, M_r, and coercivity, H_c parameters, for (a) hard and (b) soft magnetic materials.

Depending on the energies present in the system, magnetic nanostructures manifest certain reversal modes under a reversing field. Figure 3.8 depicts the dominant reversal modes, coherent, curling, and buckling, in a system with uniaxial anisotropy. In the coherent reversal mode, the magnetic moments uniformly follow the reversed external field. This mode occurs for systems where the exchange coupling between magnetic moments is strong, and any magnetic non-uniformity in the system costs considerable energy. Figure 3.8(b) shows a second reversal mode, the curling mode, where the magnetization forms a vortex-like state where the moments are parallel to the surface, avoiding the increase in the stray field as rotating away from the easy axis. This mode occurs where the increase in the exchange energy due to the vortex-like states is not considerable and, at the same time, splitting into domains is not fully favorable. Buckling (Figure 3.8(c)) is the third mode, less reported than the other two, and can be considered as a combination of the coherent and curling modes.

The reversal mechanism also depends on the magnetic system's size. The correlation between the size of nanoparticles and the reversal mechanism can be explained using the size dependency of the nucleation field shown in Figure 3.8(d). The nucleation field is the field in which the first deviations from a fully magnetized sample occur when the saturation field is lowered. Figure 3.9 also depicts the correlation of the coercivity and the magnetization states to the particle diameter.

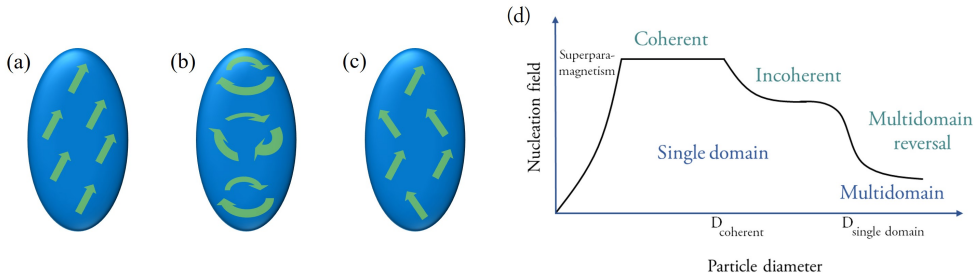

Figure 3.8: Magnetization reversal modes in nanoparticles with uniaxial anisotropy, (a) coherent, (b) curling, and (c) buckling. (d) Size dependency of reversal modes (adopted from Ref[84]).

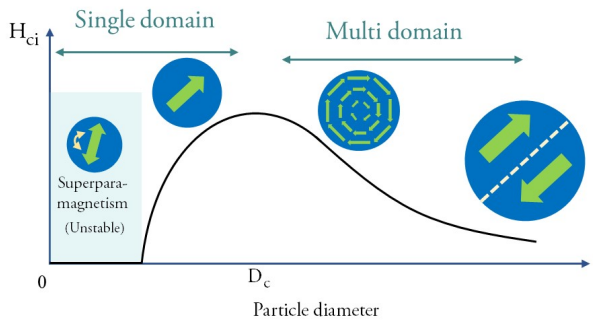

Figure 3.9: Intrinsic coercivity per particle diameter (adopted from Ref[85]). D_c is the single-domain critical diameter.

Looking beyond single particles and considering an assembly of interacting particles, such as chains, creates a special condition where particles maintain their intrinsic properties while being under the influence of the nearby particles. As an example, Figure 3.10 displays the simulated coercivity of Co-fcc nanochains of various lengths and with different interparticle crystallographic orientations and magnetic interactions **Paper I**. As can be seen, the coercivity increases as more particles are added due to the emergence of a uniaxial shape anisotropy, reaching a plateau at a chain length of about 300 nm. The graph also demonstrates how the crystallographic orientation, and consequently the MCA, of the nanoparticles along the chain affect the coercivity. In this case, having the same crystallographic orientation and the MCA aligned with the chain axis results in a larger coercivity than having a random orientation. Finally, fusing the interparticle junctions to form nanowire-like structures leads to a partially crystallographic alignment and changes the dominant interactions from dipolar to exchange and a significantly enhanced coercivity.

Unlike domain formation in nanoparticles and cylindrical nanowires, which is studied in good detail, domain formation in particle assemblies is largely absent in the literature and requires further investigation to fully understand the underlying mechanisms. To address this, the current study emphasizes the investigation of magnetization reversal and domain

formation of single nanochains in **Paper I** and **VI**, combining X-ray microscopy (Section 4.2.1) and simulations. As an example, Figure 3.11 shows simulated magnetization reversal results from a nanochain with realistic morphology. The results reveal a complex magnetization reversal process in which regions with several or larger nanoparticles facilitate the switching, while smaller particles act as pinning sites, hindering domain propagation.

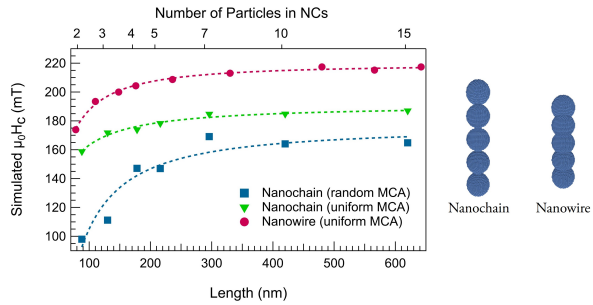

Figure 3.10: Simulated coercivity of nanochains and nanowires per length. Retrieved from **Paper I**.

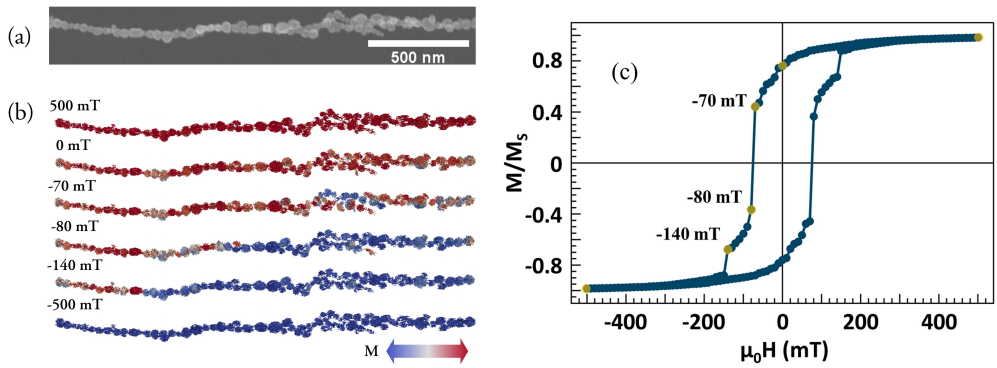

Figure 3.11: (a) SEM image of an experimentally produced nanochain, (b) Simulated magnetization reversal of a nanochain modeled from the SEM image, demonstrating nonuniform reversal behavior. (c) Simulated hysteresis loop of the structure showing a remanent magnetization, with highlighted data points corresponding to the visualized magnetization states. Taken from **Paper VI**.

3.4 Magnetoresistance

Magnetoresistance (MR) is the variation in a material's electrical resistance caused by changes in its magnetic state. In magnetic materials, the electrical resistance varies depending on the relative orientation of the electric current and the magnetization. This effect is known as anisotropic magnetoresistance (AMR), which leads to a 2-5% change in the system's resistance.

Larger MR has been observed in systems where nonmagnetic conducting spacers separate magnetic regions in the form of multilayers[86, 87]. In these systems, when the magnetic states of two magnetic layers are parallel, electrons experience a lower resistance than the antiparallel configuration. The non-magnetic spacers decouple the magnetic layers so that they can reverse their magnetization independently. The basis of this effect, called GMR, is the spin-dependent scattering of electrons passing through magnetic layers. In 3*d* transition metals, the conductance is dominated by the *s* electrons, and the resistance is mainly due to scattering of these electrons into empty *d* states near the Fermi energy. Most elastic collisions conserve spin, and the conduction channels composed of electrons with spin-up and spin-down can be considered independent (two-channel model). In a ferromagnet, the majority electrons have a spin direction antiparallel to the magnetization, see FM layer in Figure 3.12(a). As demonstrated in Figure 3.12(b), if two ferromagnetic layers, FM1 and FM2, are magnetized in the same direction, *s* electrons with spins antiparallel to the magnetic moments have a low probability of being scattered as there are few available empty majority states in the *d* band. Consequently, it is mainly *s* electrons with minority spins that scatter as they are transported through the layered system, leading to a lower resistance. In contrast, if the two layers are magnetized in the opposite directions, the majority electrons in FM1 are minority electrons in FM2 and vice versa, leading to an overall higher scattering and resistance.

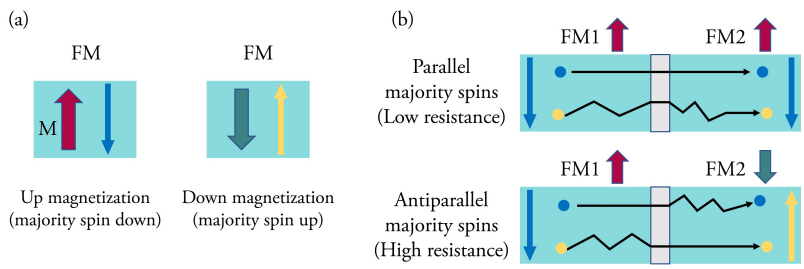

Figure 3.12: (a) Ferromagnetic layer (FM) showing the antiparallel alignment of magnetization and electrons with majority spins. (b) FM1 and FM2 layers with a nonmagnetic conducting spacer, illustrating the scattering of spin-up and spin-down *s* electrons in parallel and antiparallel majority spin configurations resulting in low and high resistance, respectively.

Employing sufficiently thin insulating spacers leads to tunneling magnetoresistance (TMR),

which exhibits greater MR compared to GMR[88]. Besides multilayer structures, this effect is observed in granular systems where magnetic nanoparticles are embedded in an insulating matrix or where there are small gaps between particles[89]. The TMR effect relies on the spin-dependent quantum-mechanical tunneling of electrons through the insulating barriers[90]. Figure 3.13(a),(b) displays schematics of the band structure of the two magnetic layers with a tunnel barrier between them. In this illustration, when the magnetization of the two ferromagnetic layers is parallel, there are plenty of available minority electrons and empty minority states at the Fermi energy to tunnel between. If, instead, the two layers are magnetized in opposite directions, the majority spins in the first layer tunnel to the minority states in the second and vice versa, leading to an increase in the resistivity as there are fewer available electrons and empty states. Similar to the scattering events in GMR, tunneling is assumed to preserve the electron spin.
Assemblies of nanoparticles are intriguing candidates for the study and use of TMR, since in these structures the tunnel barrier forms naturally as the result of interparticle gaps and not as a secondary material. Although a combination of MR effects can be present in the nanochains studied in this thesis, TMR is likely the dominant effect as small gaps separate the nanoparticles. In this work, MR is used as a tool for studying the magnetization reversal as it is highly sensitive to changes in the magnetic configuration of nanostructures. To measure MR from single or multiple nanochains, magnetic nanoparticles were directly self-assembled across source-drain gold contacts with desired dimensions prepared by electron-beam lithography as shown in Figure 3.14 (**Paper I** and **VI**).

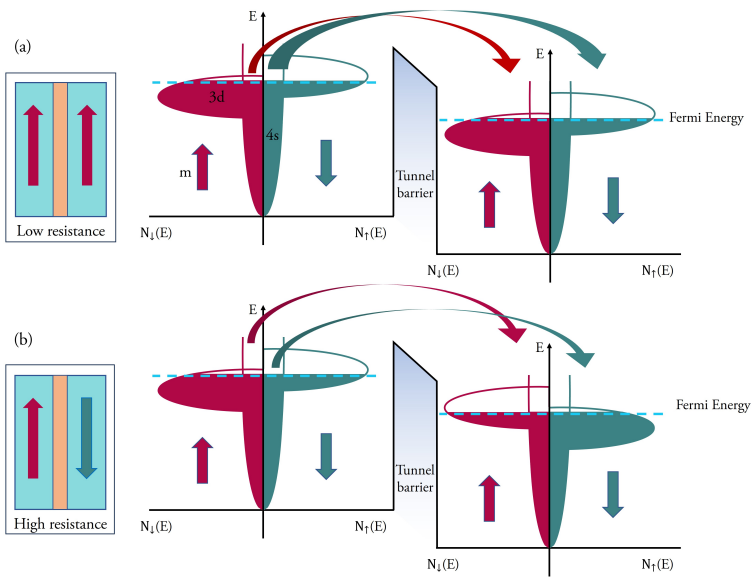

Figure 3.13: Band structure schematic of two ferromagnetic regions separated by a tunnel barrier in (a) parallel, and (b) antiparallel configurations illustrating the low and high electrical resistances, respectively. Here, the colored arrows represent the magnetic moment of electrons.

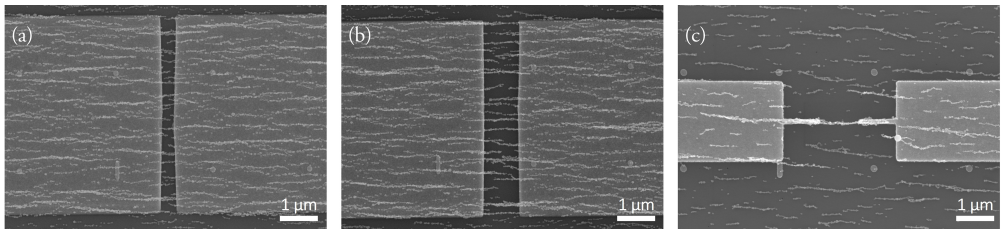

Figure 3.14: Magnetoresistive devices fabricated by the self-assembly of Co nanoparticles on source-drain terminals (a) multiple nanochains on a 500 nm gap, (b) multiple nanochains on a 1 μm gap, and (c) an individual nanochain over a 1 μm gap. Reproduced from **Paper I** and **VI**.

MR measurements on single nanochains showed that magnetization reversal in each chain is unique. However, a common behavior observed for these structures is composed of a negative response around the nucleation field and a positive response at the coercive field. Figure 3.15(a) and (b) show the SEM image and the MR response of the corresponding structure, respectively. The negative MR response can be correlated to the formation of a transverse magnetization component with regard to the current, and an increase in the resistance can be explained by the formation of domains with antiparallel magnetization. The contributions of these effects vary depending on the nanochain device, resulting in different MR behaviors. In addition, the anisotropy of the MR response was explored by performing the MR measurements at a series of angles from 0° to 360° as shown in Figure 3.15(c). The results demonstrate the effect of shape anisotropy on the magnetization reversal.

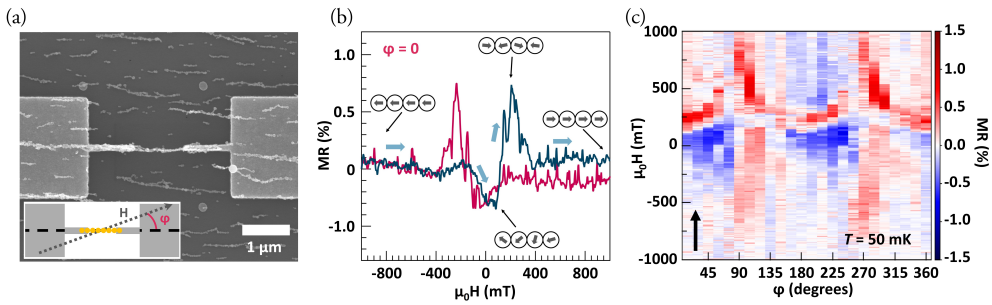

Figure 3.15: (a) SEM image of a single Co nanochain device with 1 μm gap between the source and drain. (b) MR measured under a constant DC voltage of 2 V, with the magnetic field varied along the chain axis ($\varphi = 0$) at 50 mK. (c) Angular dependence of MR, sweeping the field from -1 to 1 T at different φ angles. Retrieved from **Paper VI**.

Chapter 4

Experimental Techniques and Simulation Tools

As described in Chapter 3, materials' structural and magnetic properties are strongly coupled. Thus, a detailed study of the crystal structure and magnetic behavior of the self-assembled structures is necessary. In this work, electron microscopy is used to investigate the morphology, crystal structure, and chemical composition of the nanostructures. X-ray diffraction is utilized to further understand the crystal structure of the samples. Magnetometry is used to obtain the magnetization curves of samples through different measurement protocols, and synchrotron X-ray microscopy with magnetic contrast is implemented to image magnetic domains in single nanochains. Additionally, magnetotransport properties of nanochains are probed by electrical measurements on devices made by electron lithography. The following is an introduction to the experimental methods used in this work.

4.1 Electron Microscopy

Electron microscopy is an essential and widely used technique for imaging nanoscale structures. Unlike conventional light-based microscopes, electron microscopes employ a focused beam of electrons to probe samples. This preference for electrons over light stems from the significantly smaller de Broglie wavelength of electrons compared to photons, which provides a much higher resolution. There are two main types of electron microscopes, known as scanning electron microscopes (SEMs) and transmission electron microscopes (TEMs). Generally, SEMs are used to probe the morphology of nanostructures with a resolution in the order of a few nanometers, while TEMs provide information about the crystal structure of materials with a resolution on the order of angstroms.

4.1.1 Scanning Electron Microscopy

Scanning electron microscopes (SEMs) consist of a column where electrons are generated at the upper end and accelerated towards the lower end, where the sample is positioned. To obtain high-quality images, it is crucial to have a precisely shaped and focused electron beam directed onto the sample. This is achieved by employing electromagnetic lenses along the beam path as shown in Figure 4.1(a). SEMs typically operate with accelerating voltages of 1 to 30 kV, chosen based on the sample properties and the desired information. In SEMs, the electron beam is used to raster scan a small area of the sample, and the signal, coming from electrons emitted or reflected from the sample, is detected, and an image of the area is achieved. As the material is exposed to a high-energy electron beam, among all the emitted species, two main categories of electrons are released from the exposed area: secondary (SE) and backscattered (BSE) electrons. Secondary electrons exist in the conduction or valence band of the sample and are emitted as the material is exposed to the electron beam. However, backscattered electrons are the electrons that reflect back from the sample through the elastic interaction of the incoming electron beam and the material. While secondary electrons provide information about the topography of the sample, backscattered electrons are sensitive to the atomic number of regions within a sample.
In this work, SEM is used to image the magnetic structures to study their morphology. Moreover, identical-location SEM imaging is used to follow the self-assembly process particle by particle, by repeatedly imaging the same region of the substrate at different deposition coverages, allowing direct observation of structural evolution over time.

4.1.2 Transmission Electron Microscopy

Transmission electron microscopes (TEMs) use a more sophisticated electron column that generates and shapes a fine electron beam, typically with energies in the range of 80-300 kV. The higher electron energy leads to enhanced resolution in TEMs compared to SEMs. In TEMs, a relatively wide electron beam transmits through a thin sample (typically below 200 nm thickness), and the image or diffraction pattern of the sample is acquired by a set of electromagnetic lenses placed below the sample area as depicted in 4.1(b). Figure 4.2 shows examples of high-resolution TEM images from Co nanoparticles. Additionally, this microscope can operate in scanning mode, known as scanning transmission electron microscopy (STEM). In STEM, a focused electron beam scans across the sample, and the information is gathered through the detection and analysis of either scattered electrons or emitted characteristic X-rays from each scanned point. The STEM mode of operation can be coupled to an energy-dispersive X-ray spectrometry (XEDS) detector to analyze the emitted X-rays from the material and obtain the chemical composition of the scanned area. In this work, TEM is implemented to acquire high-resolution images of the crystal structure of nanoparticles, and STEM-XEDS is utilized to study the composition of the structures.

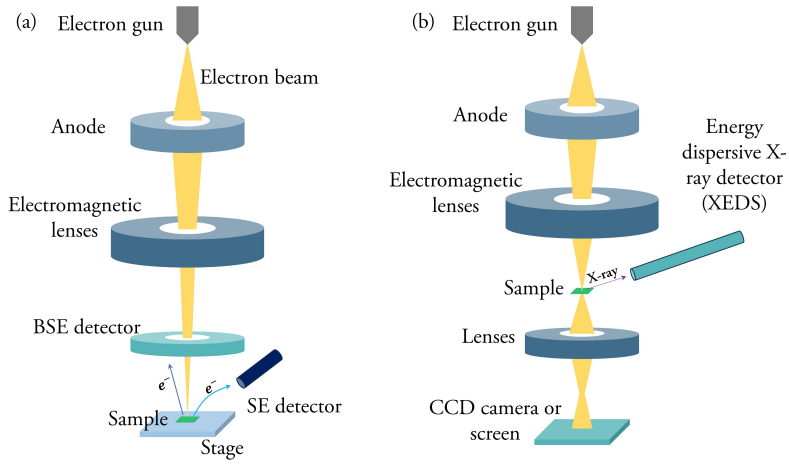

Figure 4.1: Schematic of (a) scanning electron microscope with SE and BSE detectors, and (b) transmission electron microscope equipped with an XEDS detector.

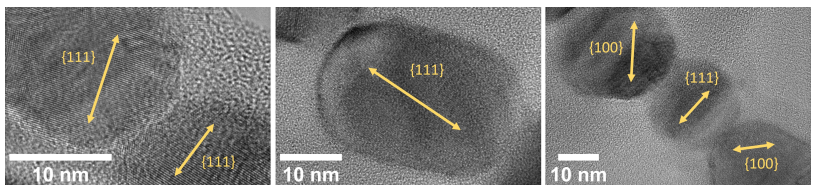

Figure 4.2: High-resolution TEM images of Co nanoparticles and their orientation with regards to each other. Sourced from the supplementary information of **Paper I**.

4.2 X-Ray Based Techniques

4.2.1 Scanning Transmission X-Ray Microscopy

Scanning transmission X-ray microscopy (STXM) employs a nano-focused X-ray beam in which the sample is raster scanned across, and the transmitted intensity from each point is detected to produce an absorption image of the sample. A schematic of STXM composed of a zone plate, order sorting aperture (OSA), raster scanning stage, and point detector is shown in Figure 4.3. The zone plate is a diffractive optical element that focuses X-rays onto the sample. It consists of a circular grating made of concentric rings with varying widths, designed to function as an X-ray lens. The alternating transparent and opaque zones diffract the incoming X-rays and create an interference pattern that focuses the X-rays to a small spot. The order sorting aperture, which is placed after the zone plate, blocks unwanted diffraction orders from the zone plate. The sample holder, mounted on a high-precision raster scanning stage, holds the sample in place and moves it with nanometer precision

relative to the focused X-ray beam. The stage scans the sample point-by-point across the beam, allowing the system to build up an absorption image by detecting transmitted X-rays at each position using a detector.

Figure 4.4 (a) and (b) show an SEM and STXM image of the same Co nanochains. Recording and integrating the total absorption from STXM images of an object obtained at different photon energies provides nano X-ray absorption spectra (XAS), as shown in Figure 4.4(c). In this example, the XAS is recorded at the Co L_3 edge corresponding to excitation of the $2p$ core-level to unoccupied $3d$ valence states. The ability to tune the X-ray energy to a specific absorption edge enables element specificity and allows for imaging with spatially resolved elemental contrast. An example of such measurement is demonstrated in Figure 4.4(d), where the FeNi and FeCo regions of the chains are identified by analyzing image stacks acquired over a range of energies around the Co and Ni L_3 edges.

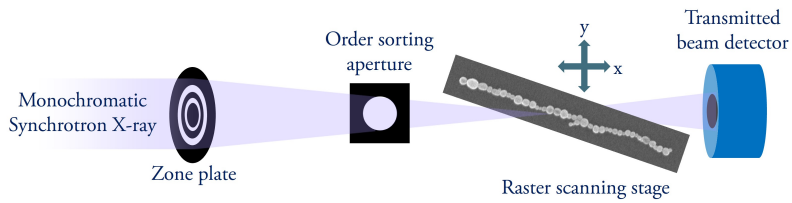

Figure 4.3: Schematic of scanning transmission X-ray microscope composed of a zone plate, OSA, sample stage, and point detector in front of an energy-selected X-ray beam.

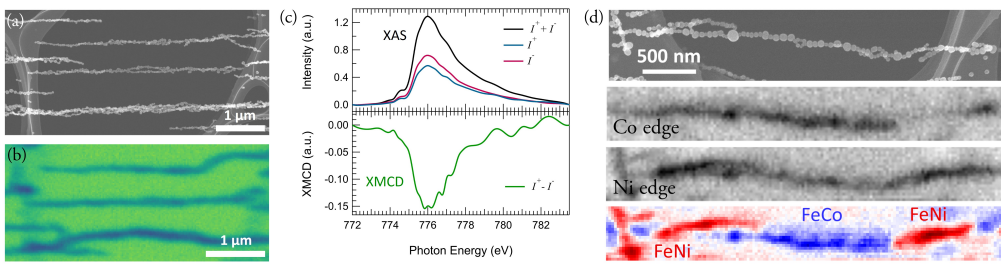

Figure 4.4: (a) SEM and (b) STXM images of the same Co nanochains. (c) Polarization dependent XAS at the Co L_3 edge obtained using right (I^+) and left (I^-) polarizations together with the total XAS ($I^+ + I^-$) and XMCD ($I^+ - I^-$) spectra. (d) SEM image of a multi-segmented sample composed of FeNi and FeCo alloy nanoparticles, together with STXM image at the Co and Ni L_3 edges, with chemical contrast obtained from analyzing image stacks.

The magnetism of the elemental and alloyed ferromagnets studied in this thesis is governed by the $3d$ valence electrons. The magnetic moment of the $3d$ valence state can be probed using circular polarized X-rays that lead to spin-dependent $2p \rightarrow 3d$ excitations. Here, right circular polarized X-rays excite 25% spin-up and 75% spin-down electrons from the $2p_{1/2}$ state (L_2 edge), and 62.5% spin-up and 37.5% spin-down from the $2p_{3/2}$ state (L_3 edge). The opposite spin-polarization is obtained using left circular polarized X-rays. There

is no difference in absorption between the two helicities for a non-magnetized sample since the valence band has an equal number of available spin-up and spin-down states. However, in the presence of the exchange splitting in the $3d$ valence bands, there will be an imbalance between the empty states with spin-up and spin-down and a difference in intensity in the absorption spectra from the two helicities (Figure 4.5). The difference in absorption between right and left circular polarized photons provides an XMCD spectrum (Figure 4.4(c)) from which the spin and orbital moments of the valence states can be quantitatively determined using so-called sum rules[91]. In this work, another feature of the XMCD spectra is explored, namely that the maximum intensity is proportional to the $3d$ magnetization projected onto the direction of the X-ray beam.

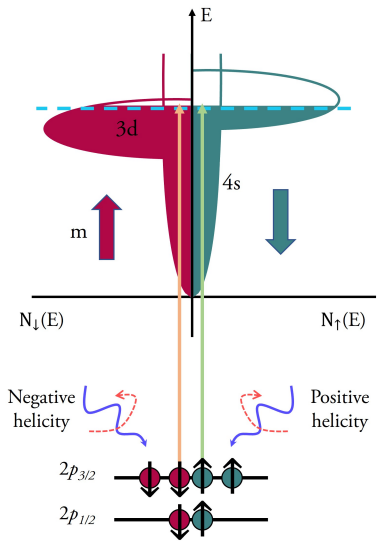

Figure 4.5: Transitions from a $2p$ core-level to the $3d$ valence, where the availability of spin-up and spin-down states differ, leading to a variation in the absorption of right and left circularly polarized X-rays, giving rise to the XMCD effect. $N_\downarrow$ and $N_\uparrow$ schematically illustrates the density of states with spin-down and up electrons. Note that the spin direction is preserved in the absorption process and that the majority electrons giving rise to the magnetization have opposite spin to the magnetization direction.

When combining STXM and XMCD, one can obtain spatially resolved magnetic contrast, which allows the study of magnetic domains and magnetization reversal at the nanoscale. Figure 4.6 shows SEM, STXM, and STXM-XMCD images of Co nanochains deposited on a TEM grid, **Paper VI**. STXM-XMCD images of the region, at the Co L_3-edge, are acquired by taking two absorption images with right and left helicities and then superimposing and subtracting them. Figure 4.6(d) shows a top view of the measurement geometry used in this work, together with the direction of the *in situ* magnetic field. The sample was mounted at a 30-degree angle with respect to the X-ray beam to probe the magnetization along the nanochains.

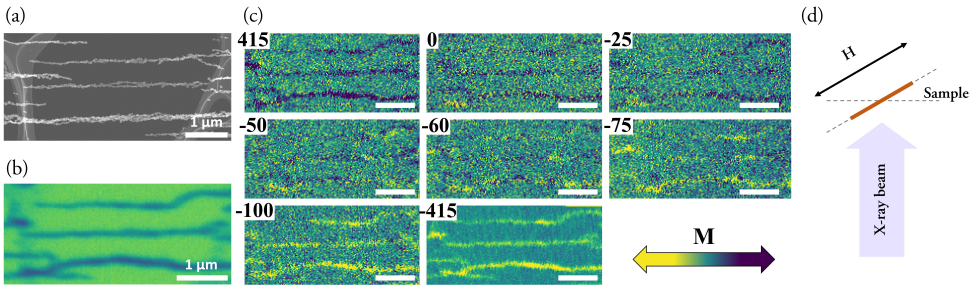

Figure 4.6: (a) SEM and (b) X-ray absorption image of an identical area of the sample. (c) STXM with magnetic contrast acquired under different magnetic fields ranging from $+415$ to -415 mT, along the nanochains, depicting magnetization reversal in the chains (scale bars = 1 µm). (d) Top view of the STXM-XMCD measurement geometry. Taken from **Paper VI**.

4.2.2 X-ray Diffraction

X-ray diffraction (XRD) is a powerful technique for the structural characterization of crystalline materials. When a material is exposed to an X-ray beam, the beam interacts with the electrons localized to the ions in the crystal. These elastic interactions cause the atoms to emit secondary waves propagating in concentric spherical wavefronts. In a crystalline structure where atoms are arranged in a highly ordered periodic fashion, these emitted waves interfere constructively or destructively, depending on their phase relationships. Constructive interference gives rise to observable diffraction peaks when the path difference, $2d\sin(\theta)$, between X-rays scattered from adjacent planes equals an integer multiple of the X-ray wavelength, which is known as the Bragg's law expressed as:

$$2dsin(\theta) = n\lambda$$

where n is an integer representing the order of reflection, λ is the wavelength of the incident X-rays, d is the distance between adjacent atomic planes in the crystal (interplanar spacing), and θ is the angle of incidence of the X-rays, see Figure 4.7(a). Information about the crystal structure, including the lattice parameters, atomic positions, and symmetry, can be extracted by analyzing the angles and intensities of these diffraction peaks. Figure 4.7(b) shows an example of an XRD pattern from FeCo nanoparticles. As opposed to TEM analysis done on individual nanoparticles, XRD patterns provide an ensemble-averaged analysis of the nanoparticles, and the sample is explored on a millimeter scale.

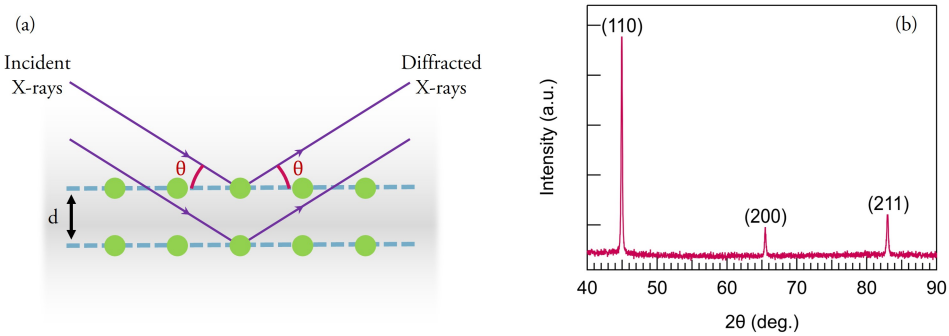

Figure 4.7: (a) A schematic showing the scattering of X-rays from a part of a crystal lattice. (b) XRD pattern obtained from FeCo alloy nanoparticles (sourced from **Paper II**).

4.3 VSM-Magnetometry

Vibrating Sample Magnetometry (VSM) is a widely employed approach for quantifying the magnetization of materials as a function of parameters like magnetic field or temperature. In the VSM setup, the sample undergoes controlled vibrations within close proximity to a set of coils known as pick-up coils. The vibration of the sample maintaining magnetization produces a time-varying magnetic field on the coil, which results in the induction of current into the circuit. The induced signal in the coil is then analyzed and interpreted as a magnetic moment. The winding of the coils is designed to remove background noises from the signal effectively. The analysis of the signal is typically performed through two methods, the standard lock-in amplifier technique for measuring the induced current in the coils or the superconducting quantum interference device (SQUID). The latter method provides a much higher sensitivity as it utilizes superconducting loops and Josephson junction principles in quantifying the signal, and thus, samples with low magnetic moments can be investigated. A schematic of a SQUID-VSM is depicted in Figure 4.8.

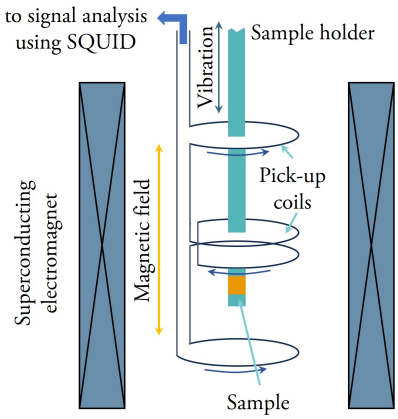

Figure 4.8: Schematic of a SQUID-VSM device for measuring magnetization.

4.4 Nanofabrication

4.4.1 Electron-Beam Lithography

Creating well-defined nanoscale features on a substrate is essential for many studies within nanotechnology. Electron beam lithography (EBL) is a versatile technique that can be used to achieve this. As shown in Figure 4.9, in this technique, first, the substrate is coated with a polymer layer with the desired thickness called the resist layer. Then, a focused electron beam, similar to SEM, is employed to precisely expose the desired parts of the resist to locally manipulate the solubility of the polymer. After this, a development solution is used to wash away the areas with higher solubility (the exposed areas), and the substrate with patterned resist goes under a thin film deposition. Finally, by dissolving the resist, the excess film layer is lifted off, and the substrate remains with the desired pattern as a metal layer.
In this study, EBL is used to fabricate electrodes needed for transport measurements. Notably, since the presented self-assembly method allows the direct deposition of nanoparticles on most substrates, a straightforward approach is developed for the transport measurements, where first the contacts are made, and then the magnetic nanoparticles are self-assembled across the gaps between the source and drain.

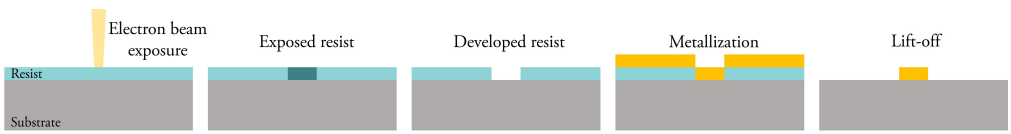

Figure 4.9: A cross-sectional view of EBL process.

4.4.2 Transport Measurements

Transport measurements are performed by probing the resistance of the samples under a constant bias voltage while sweeping the magnetic field magnitude or direction. Pre-patterned substrates comprising 24 device fields are used, and further EBL processing is performed to add contacts with desired shapes and sizes to the substrates. After that, the self-assembly of particles on the pre-made contacts is carried out. The connectivity of the devices is then first checked at room temperature using a probe station, and for conducting magnetoresistance measurements, the chips are packaged and wire-bonded onto suitable carriers. Figure 4.10 illustrates an example of such chips. Additionally, Figure 4.11, shows the device fabrication approach with before and after deposition images on a different contact design. When the chip is ready, it is loaded into the measurement system, and the analysis is carried out. The measurements are performed in a dilution refrigerator equipped with a superconducting 9-1-1 T vector magnet. To run the superconducting magnet, the devices are cooled down to the base temperature of the refrigerator, around 20 mK.

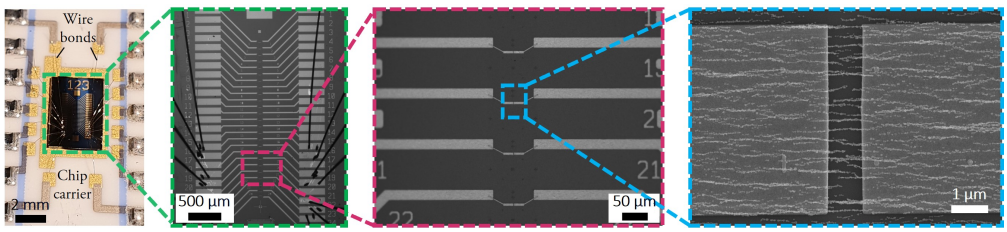

Figure 4.10: A packaged and wire-bonded chip prepared for the measurements, comprising of 7 two-terminal bonded devices.

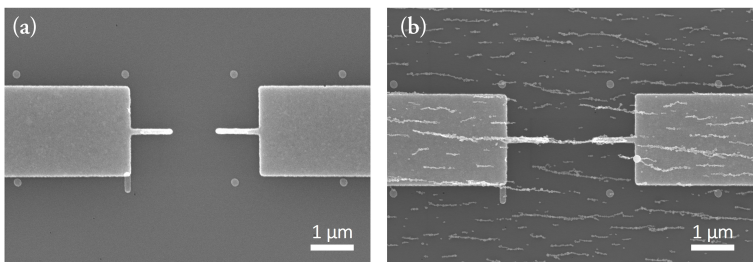

Figure 4.11: A device fabricated by deposition on pre-made connections with a 1 µm gap distance, (a) before and (b) after the nanoparticle deposition.

4.5 Micromagnetism as a Computational Tool

Micromagnetic simulation is a powerful tool for describing magnetization processes in the sub-micron scale[92]. Micromagnetics integrates quantum mechanical effects such as exchange energy, essential for ferromagnetism, within a classical continuous vector field. This semi-classical theory resolves magnetic domains and domain-wall structures, enabling accurate computation of hysteresis and equilibrium states of magnetic structures[92, 93]. Additionally, magnetization dynamics can be described using the Landau-Lifshitz-Gilbert equation on the picosecond timescale[92, 94, 95, 96].
Micromagnetics considers the magnetic material to be made up of discrete blocks with a homogeneous spin density and constant magnetization described by a vector field

$$\vec{M}(x) = M_s \vec{m}(x) \quad with \ |\vec{m}(x)| = 1,$$

where M_s is the spontaneous magnetization, which at zero temperature simulations is the saturation magnetization, and x represents the position. As an example, Figure 4.12(a) shows a discretized space of $20 \times 10 \times 1$ nm³ composed of $1 \times 1 \times 1$ nm³ cells. In Figure 4.12(b), the associated $\mathbf{M}(x)$ for each cell is illustrated forming the vector field. Thus, micromagnetics considers the interactions between a discrete set of blocks instead of individual spins, simplifying the calculations and providing a cost-efficient simulation of magnetic structures up to a few microns.

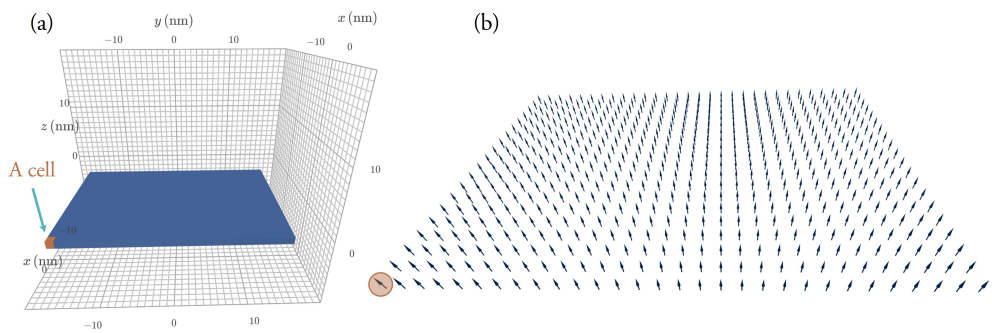

Figure 4.12: (a) A $20 \times 10 \times 1$ nm³ discretized magnetic layer composed of cells, (b) vectors assigned to each cell building up the vector field.

Micromagnetic simulations can be performed mainly in two modes, depending on the purpose of the study, known as dynamic and static simulations. The latter is used in this thesis, where the stable magnetization configuration at a given magnetic field is obtained by minimizing the total energy of the system. For a nanochain structure, the total energy density can be expressed as

$$E_{tot} = A(\nabla \vec{m})^2 - K_1 \left[\vec{m_1}^2 \vec{m_2}^2 + \vec{m_2}^2 \vec{m_3}^2 + \vec{m_1}^2 \vec{m_3}^2 \right] - \frac{1}{2}\mu_0 \vec{M} \cdot \vec{H}_d - \mu_0 M_s \vec{m} \cdot \vec{H}$$
$$\text{with } m_i = m \cdot u_i \quad (i = 1, 2, 3).$$

The first term represents the exchange interaction, the second term accounts for the magnetocrystalline anisotropy with u_i being the unit vectors defining the easy axes of the cubic crystal, the third term reflects the magnetostatic energy contribution, and the final term describes the Zeeman energy. The input parameters to the energies consist of the exchange stiffness constant A, cubic anisotropy constant K_1, MCA orientations, and spontaneous magnetization M_s. In this work, micromagnetic simulations are conducted by Ubermag with OOMMF micromagnetic calculator that obtains the configuration with the nearest energy minimum using numerical optimization methods[97, 98].

In **Paper I**, and **II**, magnetic behavior of nanochains are explored through micromagnetic simulations, by designing chains as a linear arrangement of spheres with sizes around 40 nm, and cubic MCA. This type of simulation provides a general understanding of preferred magnetization states or magnetization reversal processes. However, to expand upon the effect of the morphological features of nanochains in the magnetization reversal, an algorithm is developed, presented in **Paper VI**, by which experimentally produced nanochains can be converted to 3D magnetic models, which are then fed to the micromagnetic simulations. This methodology allows for more precise simulations of nanochains and provides a better understanding of the magnetic properties of such structures, since the morphological features play a crucial role in the magnetization reversal.

The process of building magnetic models from SEM images begins with loading the image using the Open Source Computer Vision (OpenCV) library in Python. Following this, particle detection takes place. Initially, the images are prepared by thresholding to remove the background, and then the contours of the particles are detected using OpenCV's "findContours" function. Information about each detected particle, such as its center position (in x and y axes), major and minor axes lengths, and orientation angle, is extracted using "minAreaRect" which allows the reconstruction of the structure. Since the particles are mostly symmetric, the unknown depth diameter of the particles is approximated to one of the known axes. Then, adjustments are made to avoid overlapping particles by calculating the intersection of their bounding boxes. To mitigate the overlapping of the particles, they are slightly moved along the depth. Following particle detection and adjustments, a Pandas DataFrame containing particle parameters is constructed. This DataFrame serves as input for the Ubermag-OOMMF simulation framework. A schematic of the process is shown in Figure 4.13.

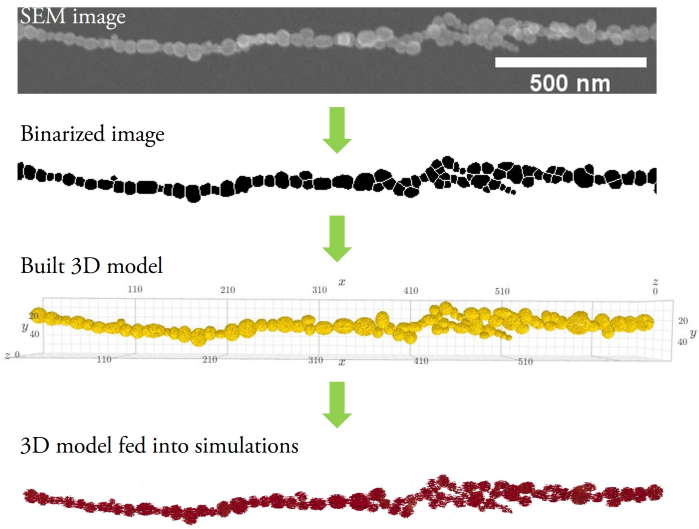

Figure 4.13: Steps involved in the image processing and building magnetic simulation models from an SEM image to a magnetic vector field. Taken from the supplementary information of **Paper VI**.

Chapter 5

Conclusions and Outlook

Studies carried out within this thesis cover a range of topics, from the production and controlled self-assembly of gas-phase generated nanoparticles to the detailed characterization of their magnetic properties and the development of nanoscale devices and magneto-responsive soft films. This chapter summarizes the main conclusions derived from different parts of the work and finishes with an outlook on potential pathways for the future.

Main Conclusions

Gas-Phase Nanoparticle Generation

In this work, different nanoparticles, particularly Co, Ni, FeCo, and FeNi, are generated. The structural characterizations show that the particles maintain high crystallinity and phase uniformity. The spark ablation method proved its versatility in producing various metallic nanoparticles with subtle variations in the production parameters. The capability of alloy nanoparticle generation is shown in two ways: co-ablating two different electrode materials and using pre-alloyed electrodes as anode and cathode. Both strategies resulted in alloys with a uniform distribution of elements in FeCo and FeNi. However, for producing nanoparticles with specific compositions, only the latter strategy can provide good control as, in this case, the nanoparticle compositions closely match the electrodes.

Controlled Self-Assembly of Nanoparticles

It is shown that the composition of chains can be tuned by the consecutive deposition of nanoparticles with different compositions, which opens the way for tuning the physical properties of these structures for various purposes. It is also demonstrated that the use of charged magnetic gas-phase nanoparticles enables control over the assembly process by adjusting the ratio of applied electric and magnetic forces on the particles during deposition. While low electric fields assemble nanoparticles into longer chains with large interchain spacing, high electric fields result in shorter chains and a more compact chain placement. The importance of this strategy is that the final structures can be tuned without adding complexities to the process, as no substrate patterning or masking is required.

Direct integration

In addition to all the capabilities of the methodology demonstrated in this work, particularly in particle generation and deposition, the thesis shows that the combination of electric and magnetic fields allows for controlled self-assembly and direct integration of charged nanoparticles on substrates. This work explores this capability by developing magneto-responsive soft films suitable for magnetic actuation and magnetoresistive devices used for magnetization reversal studies. Maintaining the anisotropic behavior of the nanochains, the films respond highly to magnetic fields. Moreover, it is demonstrated that the developed method allows for tuning the bending performance by varying the amount of deposited material and the mechanical properties of soft layers. Furthermore, this capability enables the integration of nanochains onto pre-patterned silicon chips. To the best of our knowledge, this allowed for the first magnetotransport studies of nanochains.

Magnetic Properties

This thesis studies the magnetic properties of random nanoparticle assemblies, 1D nanochains, and nanowire-like structures in detail. It is demonstrated that arranging the nanoparticles into nanochains introduces a significant shape anisotropy and that fusing the particles by post-annealing substantially influences the magnetic interactions and defines the magnetic behavior of Co nanowire-like structures.
The direct integration capability of the developed methodology allowed for studying individual nanochains using X-ray microscopy and magnetoresistance measurements. The experimental results, complemented by micromagnetic simulations, reveal that the magnetization reversal in Co nanochains follows a nonuniform switching governed by the morphology of the assembled system. Despite this, averaging the XMCD contrast over the individual structures showed that the self-assembled systems have similar magnetization

remanent and coercivity values.

Outlook

This work can be expanded in several ways concerning gas-phase production, self-assembly, and applications. One important aspect that can be developed is controlling the crystal phase of nanoparticles in-flight through suitable thermal processes, such as tuning the residence time in the furnace. This can help a better control in producing nanoparticles where the crystal structure of the material is important, such as in CoPt and FePt alloys where $L1_0$ phase formation is necessary to obtain hard magnetic properties. Controlling the crystal phase of particles in-flight can also pave the way for producing oxide nanoparticles with desired structures, which is of importance and value due to the wide applications of oxide magnetic nanomaterials.
Another interesting pathway is continuing on the characterization of multi-segmented and nanocomposite structures, focusing not only on the magnetic properties but also on the electrochemical and catalysis studies. Moreover, the nanocomposite structures are interesting from the viewpoint of electromagnetic wave shielding because of the composition control and the porous morphology of structures, which enable multiple reflections and scattering of waves.
The direct integration of self-assembled structures is one of the key aspects of this methodology. Although there is significant progress in the magnetic microactuation field using other synthesis methods, the direct integration of gas-phase nanoparticles can open up new possibilities, such as for the large-scale integration of magnetic nanostructures into soft actuators. This capability is hard to achieve using common multi-step chemical methods. Figure 5.1 displays a conceptual schematic of the continuous production of magnetic films in a roll-to-roll process, highlighting a promising direction for future development.

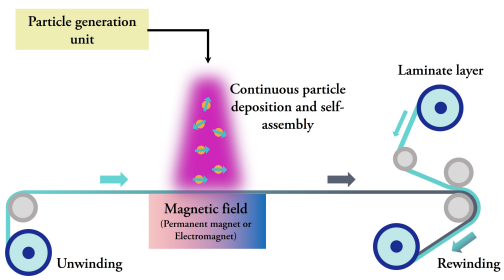

Figure 5.1: Conceptual schematic of the roll-to-roll process for the continuous fabrication of magnetic films, where a pristine polymer layer is coated by the assembly of nanoparticles and then laminated and rolled. Retrieved from **Paper V**.

Appendix

Aerosol Instruments

Bipolar diffusion charger

A bipolar diffusion charger is a device designed to establish a known charge distribution on aerosol nanoparticles through ion-particle interactions in a controlled environment. In this work, a diffusion charger with Ni^{63} radioactive source is used, which emits β radiation and ionizes the surrounding gas. The ions undergo Brownian motion and diffuse toward the nanoparticles, transferring charge upon collision. The charge distribution obtained follows a probabilistic Boltzmann equilibrium, where particles gain both positive and negative charges. As the result of ion-particle interactions in the diffusion charger, the aerosol particles consist of neutral, positively charged, and negatively charged particles with a well-defined charge distribution. The bipolar charge distribution of the particles is detailed in Ref[99]. In this work, bipolar diffusion charging is used before the size selection step, ensuring that nanoparticles maintain a predictable charge distribution.

Differential Mobility Analyzer

Differential Mobility Analyzers are widely used in aerosol technology for size-selecting nanoparticles based on their electrical mobility. DMAs comprise a chamber with two plates, *e.g.* in a concentric cylindrical geometry, between which a constant high electric field is established. As poly-disperse particles enter the DMA, a sheath gas flow carries them into the electric field and ultimately guides the particles with desired electrical mobility out through a narrow slit. As particles travel through the electric field, the ones with higher electrical mobility (smaller particles) get deposited on the plates before the outlet slit, while low-mobility particles either get deposited after the slit along the plates or exit the chamber with the sheath gas to the exhaust. Changing the electric field can change the size of particles exiting DMAs. The particles coming out of the DMA have a similar polarity,

which in this study are negatively charged particles. Positively charged particles get attracted and deposited inside the DMA, and neutral particles leave the DMA with the sheath flow to the exhaust. Figure 2 shows a simple schematic demonstrating DMA size selection principles. Electrical mobility is described by

$$z_p = \frac{neC_c}{3\pi\eta D_p}, \tag{1}$$

where n is the number of charges on the particle, e is the elementary charge, C_c is Cunningham slip correction, η is the dynamic viscosity of gas and D_p is diameter of the particle.

$$C_c = 1 + \frac{2\lambda}{D_p}\left(A_1 + A_2 e^{\frac{-A_3 D_p}{\lambda}}\right) \tag{2}$$

with λ being the mean free path, and A_n are experimentally determined coefficients.

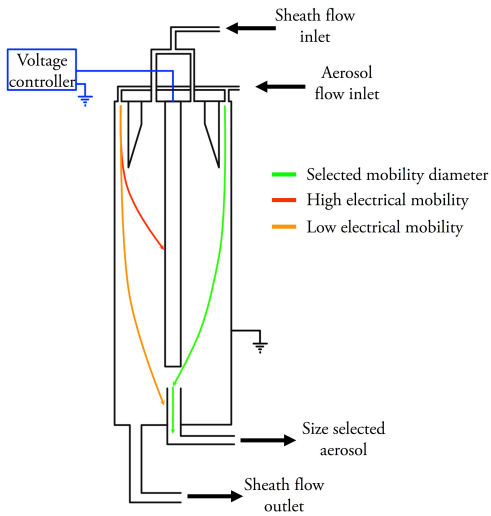

Figure 2: Schematic illustration of a DMA.

Electrometer

Electrometers play a crucial role in aerosol technology for acquiring aerosol particle concentration based on measuring the electrical charge they carry. These highly sensitive devices detect small currents generated when charged aerosol particles pass through an electrode or are collected on a filter. The electrometer estimates the particle concentration in the gas by measuring the current induced or transferred by the charged particles. This particle concentration is essential as it can be used to determine the deposition time needed to achieve a desired particle concentration on substrates.

References

[1] Srikanth Singamaneni, Valery N Bliznyuk, Christian Binek, and Evgeny Y Tsymbal. Magnetic nanoparticles: recent advances in synthesis, self-assembly and applications. *Journal of Materials Chemistry*, 21(42):16819–16845, 2011.

[2] Elsa M Materón, Celina M Miyazaki, Olivia Carr, Nirav Joshi, Paulo HS Picciani, Cleocir J Dalmaschio, Frank Davis, and Flavio M Shimizu. Magnetic nanoparticles in biomedical applications: A review. *Applied Surface Science Advances*, 6:100163, 2021.

[3] Panangattukara Prabhakaran Praveen Kumar, Md Nafiujjaman, Ashley V Makela, Kay Hadrick, Meghan L Hill, Maggie Lee, and Taeho Kim. Development of iron oxide nanochains as a sensitive magnetic particle imaging tracer for cancer detection. *ACS Applied Materials & Interfaces*, 2025.

[4] Carlos Martinez-Boubeta and Konstantinos Simeonidis. Magnetic nanoparticles for water purification. *Nanoscale materials in water purification*, pages 521–552, 2019.

[5] Samuel CN Tang and Irene MC Lo. Magnetic nanoparticles: essential factors for sustainable environmental applications. *Water research*, 47(8):2613–2632, 2013.

[6] Atsufumi Hirohata, Keisuke Yamada, Yoshinobu Nakatani, Ioan-Lucian Prejbeanu, Bernard Diény, Philipp Pirro, and Burkard Hillebrands. Review on spintronics: Principles and device applications. *Journal of Magnetism and Magnetic Materials*, 509:166711, 2020.

[7] Amalio Fernández-Pacheco, Robert Streubel, Olivier Fruchart, Riccardo Hertel, Peter Fischer, and Russell P Cowburn. Three-dimensional nanomagnetism. *Nature communications*, 8(1):1–14, 2017.

[8] Stuart SP Parkin, Masamitsu Hayashi, and Luc Thomas. Magnetic domain-wall racetrack memory. *Science*, 320(5873):190–194, 2008.

[9] Stuart Parkin and See-Hun Yang. Memory on the racetrack. *Nature nanotechnology*, 10(3):195–198, 2015.

[10] Yurii P Ivanov, Andrey Chuvilin, Sergei Lopatin, and Jurgen Kosel. Modulated magnetic nanowires for controlling domain wall motion: toward 3d magnetic memories. *ACS nano*, 10(5):5326–5332, 2016.

[11] Cristina Bran, Eider Berganza, Jose A Fernandez-Roldan, Ester M Palmero, Jessica Meier, Esther Calle, Miriam Jaafar, Michael Foerster, Lucia Aballe, Arantxa Fraile Rodriguez, et al. Magnetization ratchet in cylindrical nanowires. *Acs Nano*, 12(6):5932–5939, 2018.

[12] Tristan da Câmara Santa Clara Gomes, Nicolas Marchal, Flavio Abreu Araujo, and Luc Piraux. Spin caloritronics in 3d interconnected nanowire networks. *Nanomaterials*, 10(11):2092, 2020.

[13] Zhi-Min Liao, Ya-Dong Li, Jun Xu, Jing-Min Zhang, Ke Xia, and Da-Peng Yu. Spin-filter effect in magnetite nanowire. *Nano letters*, 6(6):1087–1091, 2006.

[14] Vladislav E Demidov, Sergei Urazhdin, Henning Ulrichs, Vasyl Tiberkevich, Andrei Slavin, Dietmar Baither, Guido Schmitz, and Sergej O Demokritov. Magnetic nano-oscillator driven by pure spin current. *Nature materials*, 11(12):1028–1031, 2012.

[15] JC Guzmán-Mínguez, S Ruiz-Gómez, LM Vicente-Arche, Cecilia Granados-Miralles, C Fernández-González, F Mompeán, M García-Hernández, S Erohkin, Dmitry Berkov, D Mishra, et al. Feco nanowire–strontium ferrite powder composites for permanent magnets with high-energy products. *ACS Applied Nano Materials*, 3(10):9842–9851, 2020.

[16] Jeotikanta Mohapatra, Meiying Xing, Jacob Elkins, Julian Beatty, and J Ping Liu. Extraordinary magnetic hardening in nanowire assemblies: the geometry and proximity effects. *Advanced Functional Materials*, 31(13):2010157, 2021.

[17] Mircea V Rastei, Véronique Pierron-Bohnes, Delphine Toulemon, Corinne Bouillet, Attila Kakay, Riccardo Hertel, Ebenezer Tetsi, Sylvie Begin-Colin, and Benoit P Pichon. Defect-driven magnetization configuration of isolated linear assemblies of iron oxide nanoparticles. *Advanced Functional Materials*, 29(45):1903927, 2019.

[18] Minsu Kang, Minho Seong, Donghyuk Lee, Seong Min Kang, Moon Kyu Kwak, and Hoon Eui Jeong. Self-assembled artificial nanocilia actuators. *Advanced Materials*, 34(24):2200185, 2022.

[19] Alexander Tokarev, Jeremy Yatvin, Oleksandr Trotsenko, Jason Locklin, and Sergiy Minko. Nanostructured soft matter with magnetic nanoparticles. *Advanced Functional Materials*, 26(22):3761–3782, 2016.

[20] Sophie Marchi, Alberto Casu, Franco Bertora, Athanassia Athanassiou, and Despina Fragouli. Highly magneto-responsive elastomeric films created by a two-step fabrication process. *ACS applied materials & interfaces*, 7(34):19112–19118, 2015.

[21] Luolin Li, Zheng Yu, Jianfeng Liu, Manyi Yang, Gongpu Shi, Ziqi Feng, Wei Luo, Huiru Ma, Jianguo Guan, and Fangzhi Mou. Swarming responsive photonic nanorobots for motile-targeting microenvironmental mapping and mapping-guided photothermal treatment. *Nano-Micro Letters*, 15(1):141, 2023.

[22] Yuting Liao, Dong Liu, Bin Wang, Zijian Wu, Miao Ni, Mengchen Wang, Cheng-Hua Wang, and Yuan Lu. Photothermally modulated magnetic nanochains as swarm nanorobotics for microreaction control. *ACS Applied Nano Materials*, 6(1):21–33, 2022.

[23] Tianlong Li, Jinxing Li, Konstantin I Morozov, Zhiguang Wu, Tailin Xu, Isaac Rozen, Alexander M Leshansky, Longqiu Li, and Joseph Wang. Highly efficient freestyle magnetic nanoswimmer. *Nano letters*, 17(8):5092–5098, 2017.

[24] Yulan Chen, Karthik Srinivasan, Marcus Choates, Ludovico Cestarollo, and Amal El-Ghazaly. Enhanced magnetic anisotropy for reprogrammable high-force-density microactuators. *Advanced Functional Materials*, 34(2):2305502, 2024.

[25] Wenbin You, Ke Pei, Liting Yang, Xiao Li, Xiaofeng Shi, Xuefeng Yu, Huiqiao Guo, and Renchao Che. In situ dynamics response mechanism of the tunable length-diameter ratio nanochains for excellent microwave absorber. *Nano Research*, 13(1):72–78, 2020.

[26] Jia Liu, Mao-Sheng Cao, Qiang Luo, Hong-Long Shi, Wen-Zhong Wang, and Jie Yuan. Electromagnetic property and tunable microwave absorption of 3d nets from nickel chains at elevated temperature. *ACS applied materials & interfaces*, 8(34):22615–22622, 2016.

[27] Sebastian Ekeroth, Joakim Ekspong, Dimitrios K Perivoliotis, Sachin Sharma, Robert Boyd, Nils Brenning, Eduardo Gracia-Espino, Ludvig Edman, Ulf Helmersson, and Thomas Wågberg. Magnetically collected platinum/nickel alloy nanoparticles as catalysts for hydrogen evolution. *ACS Applied Nano Materials*, 4(12):12957–12965, 2021.

[28] Sebastian Ekeroth, E Peter Münger, Robert Boyd, Joakim Ekspong, Thomas Wågberg, Ludvig Edman, Nils Brenning, and Ulf Helmersson. Catalytic nanotruss structures realized by magnetic self-assembly in pulsed plasma. *Nano Letters*, 18(5):3132–3137, 2018.

[29] Bin Su, Yuchen Wu, Yue Tang, Yi Chen, Wenlong Cheng, and Lei Jiang. Free-standing 1d assemblies of plasmonic nanoparticles. *Advanced Materials*, 25(29):3968–3972, 2013.

[30] Min Xiong, Xiulong Jin, and Jian Ye. Strong plasmon coupling in self-assembled superparamagnetic nanoshell chains. *Nanoscale*, 8(9):4991–4999, 2016.

[31] Xiangyu Jiang, Jiangang Feng, Lei Huang, Yuchen Wu, Bin Su, Wensheng Yang, Liqiang Mai, and Lei Jiang. Bioinspired 1d superparamagnetic magnetite arrays with magnetic field perception. *Advanced Materials*, 28(32):6952–6958, 2016.

[32] Yue Tang, Bin Su, Minsu Liu, Yuan Feng, Xuchuan Jiang, Lei Jiang, and Aibing Yu. Superwettability strategy: 1d assembly of binary nanoparticles as gas sensors. *Small*, 13(4):1601087, 2017.

[33] Dong Liu, Shangsong Li, Ting Zhang, Hao Jiang, and Yuan Lu. 3d magnetic field-controlled synthesis, collective motion, and bioreaction enhancement of multifunctional peasecod-like nanochains. *ACS Applied Materials & Interfaces*, 13(30):36157–36170, 2021.

[34] Edouard Alphandery, Stephanie Faure, Olivier Seksek, François Guyot, and Imene Chebbi. Chains of magnetosomes extracted from amb-1 magnetotactic bacteria for application in alternative magnetic field cancer therapy. *ACS nano*, 5(8):6279–6296, 2011.

[35] Serena A Corr, Stephen J Byrne, Renata Tekoriute, Carla J Meledandri, Dermot F Brougham, Marina Lynch, Christian Kerskens, Laurence O'Dwyer, and Yurii K Gun'ko. Linear assemblies of magnetic nanoparticles as mri contrast agents. *Journal of the American Chemical Society*, 130(13):4214–4215, 2008.

[36] A Fert and Luc Piraux. Magnetic nanowires. *Journal of Magnetism and Magnetic Materials*, 200(1-3):338–358, 1999.

[37] Xinlong Fan and Andreas Walther. 1d colloidal chains: recent progress from formation to emergent properties and applications. *Chemical Society Reviews*, 51(10):4023–4074, 2022.

[38] Sofía Raviolo, Felipe Tejo, Noelia Bajales, and Juan Escrig. Angular dependence of the magnetic properties of permalloy and nickel nanowires as a function of their diameters. *Materials Research Express*, 5(1):015043, 2018.

[39] Cristina Bran, Jose Angel Fernandez-Roldan, Rafael P. Del Real, Agustina Asenjo, Yu-Shen Chen, Junli Zhang, Xixiang Zhang, Arantxa Fraile Rodríguez, Michael Foerster, Lucia Aballe, et al. Unveiling the origin of multidomain structures in compositionally modulated cylindrical magnetic nanowires. *ACS nano*, 14(10):12819–12827, 2020.

[40] Michal Staňo and Olivier Fruchart. Magnetic nanowires and nanotubes. In *Handbook of magnetic materials*, volume 27, pages 155–267. Elsevier, 2018.

[41] José María De Teresa. *Nanofabrication: Nanolithography techniques and their applications*. IOP Publishing, 2020.

[42] Amalio Fernández-Pacheco, Luka Skoric, José María De Teresa, Javier Pablo-Navarro, Michael Huth, and Oleksandr V Dobrovolskiy. Writing 3d nanomagnets using focused electron beams. *Materials*, 13(17):3774, 2020.

[43] Amalio Fernández-Pacheco, Luis Serrano-Ramón, Jan M Michalik, M Ricardo Ibarra, José M De Teresa, Liam O'Brien, Dorothée Petit, Jihyun Lee, and Russell P Cowburn. Three dimensional magnetic nanowires grown by focused electron-beam induced deposition. *Scientific reports*, 3(1):1–5, 2013.

[44] Javier Pablo-Navarro, César Magén, and José María De Teresa. Purified and crystalline three-dimensional electron-beam-induced deposits: the successful case of cobalt for high-performance magnetic nanowires. *ACS Applied Nano Materials*, 1(1):38–46, 2017.

[45] César Magén, Javier Pablo-Navarro, and José María De Teresa. Focused-electron-beam engineering of 3d magnetic nanowires. *Nanomaterials*, 11(2):402, 2021.

[46] Zhiwei Li, Fan Yang, and Yadong Yin. Smart materials by nanoscale magnetic assembly. *Advanced Functional Materials*, 30(2):1903467, 2020.

[47] Linfeng Chen, Bin Su, and Lei Jiang. Recent advances in one-dimensional assembly of nanoparticles. *Chemical Society Reviews*, 48(1):8–21, 2019.

[48] Angus McMullen, Miranda Holmes-Cerfon, Francesco Sciortino, Alexander Y Grosberg, and Jasna Brujic. Freely jointed polymers made of droplets. *Physical review letters*, 121(13):138002, 2018.

[49] Delphine Toulemon, Mircea V Rastei, David Schmool, José Sáiz Garitaonandia, Luis Lezama, Xavier Cattoën, Sylvie Bégin-Colin, and Benoit P Pichon. Enhanced collective magnetic properties induced by the controlled assembly of iron oxide nanoparticles in chains. *Advanced Functional Materials*, 26(15):2454–2462, 2016.

[50] Jun Wang, Qianwang Chen, Chuan Zeng, and Binyang Hou. Magnetic-field-induced growth of single-crystalline fe304 nanowires. *Advanced Materials*, 16(2):137–140, 2004.

[51] Wen Zhang, Ping Kwan Johnny Wong, Dong Zhang, Jinjin Yue, Zhaoxia Kou, Gerrit van der Laan, Andreas Scholl, Jian-Guo Zheng, Zuhong Lu, and Ya Zhai. Xmcd and xmcd-peem studies on magnetic-field-assisted self-assembled 1d nanochains of spherical ferrite particles. *Advanced Functional Materials*, 27(29):1701265, 2017.

[52] Zhaoxia Kou, Er Liu, Jinjin Yue, Yunxia Sui, Zhaocong Huang, Dong Zhang, Yukun Wang, Ya Zhai, Jun Du, and Hongru Zhai. The magnetic properties of well-aligned nickel nanochains synthesized by magnetic field-induced assembly approach. *Journal of Applied Physics*, 117(17):17E709, 2015.

[53] Y Zhang, L Sun, Y Fu, ZC Huang, XJ Bai, Y Zhai, J Du, and HR Zhai. The shape anisotropy in the magnetic field-assisted self-assembly chain-like structure of magnetite. *The Journal of Physical Chemistry C*, 113(19):8152–8157, 2009.

[54] Guangjun Cheng, Danilo Romero, Gerald T Fraser, and AR Hight Walker. Magnetic-field-induced assemblies of cobalt nanoparticles. *Langmuir*, 21(26):12055–12059, 2005.

[55] Yulan Chen and Amal El-Ghazaly. Self-assembly of magnetic nanochains in an intrinsic magnetic dipole force-dominated regime. *Small*, page 2205079, 2022.

[56] Ping Liu, Zijiong Li, Bo Zhao, Boluo Yadian, and Yafei Zhang. Template-free synthesis of nickel nanowires by magnetic field. *Materials Letters*, 63(20):1650–1652, 2009.

[57] Tobias Kraus, Laurent Malaquin, Heinz Schmid, Walter Riess, Nicholas D Spencer, and Heiko Wolf. Nanoparticle printing with single-particle resolution. *Nature nanotechnology*, 2(9):570–576, 2007.

[58] Bin Su, Cong Zhang, Shuoran Chen, Xingye Zhang, Linfeng Chen, Yuchen Wu, Yiwen Nie, Xiaonan Kan, Yanlin Song, and Lei Jiang. A general strategy for assembling nanoparticles in one dimension. *Advanced Materials*, 26(16):2501–2507, 2014.

[59] Jicheng Feng, Dong Chen, Peter V Pikhitsa, Yoon-ho Jung, Jun Yang, and Mansoo Choi. Unconventional alloys confined in nanoparticles: Building blocks for new matter. *Matter*, 3(5):1646–1663, 2020.

[60] Wooik Jung, Yoon-Ho Jung, Peter V Pikhitsa, Jicheng Feng, Younghwan Yang, Minkyung Kim, Hao-Yuan Tsai, Takuo Tanaka, Jooyeon Shin, Kwang-Yeong Kim, et al. Three-dimensional nanoprinting via charged aerosol jets. *Nature*, 592(7852):54–59, 2021.

[61] Damien P Debecker, Solène Le Bras, Cédric Boissière, Alexandra Chaumonnot, and Clément Sanchez. Aerosol processing: a wind of innovation in the field of advanced heterogeneous catalysts. *Chemical Society Reviews*, 47(11):4112–4155, 2018.

[62] GH Lee, SH Huh, JW Park, H-C Ri, and JW Jeong. Arrays of ferromagnetic iron and cobalt nanocluster wires. *The Journal of Physical Chemistry B*, 106(9):2123–2126, 2002.

[63] EK Athanassiou, P Grossmann, RN Grass, and Wendelin J Stark. Template free, large scale synthesis of cobalt nanowires using magnetic fields for alignment. *Nanotechnology*, 18(16):165606, 2007.

[64] Calle Preger, Martin Josefsson, Rasmus Westerström, and Maria E Messing. Bottom-up field-directed self-assembly of magnetic nanoparticles into ordered nano-and macrostructures. *Nanotechnology*, 32(19):195603, 2021.

[65] George Biskos, Vincent Vons, Caner U Yurteri, and Andreas Schmidt-Ott. Generation and sizing of particles for aerosol-based nanotechnology. *KONA Powder and Particle Journal*, 26:13–35, 2008.

[66] Andreas Schmidt-Ott. *Spark Ablation: Building Blocks for Nanotechnology*. CRC Press, 2019.

[67] N Salman Tabrizi, Q Xu, NM Van Der Pers, and A Schmidt-Ott. Generation of mixed metallic nanoparticles from immiscible metals by spark discharge. *Journal of Nanoparticle Research*, 12:247–259, 2010.

[68] Jicheng Feng, Nabil Ramlawi, George Biskos, and Andreas Schmidt-Ott. Internally mixed nanoparticles from oscillatory spark ablation between electrodes of different materials. *Aerosol Science and Technology*, 52(5):505–514, 2018.

[69] Pau Ternero, Mehran Sedrpooshan, David Wahlqvist, Bengt O Meuller, Martin Ek, Julia-Maria Hübner, Rasmus Westerström, and Maria E Messing. Effect of the carrier gas on the structure and composition of co–ni bimetallic nanoparticles generated by spark ablation. *Journal of Aerosol Science*, 170:106146, 2023.

[70] Calle Preger, Claudiu Bulbucan, Bengt O Meuller, Linus Ludvigsson, Aram Kostanyan, Matthias Muntwiler, Knut Deppert, Rasmus Westerström, and Maria E Messing. Controlled oxidation and self-passivation of bimetallic magnetic fecr and femn aerosol nanoparticles. *The Journal of Physical Chemistry C*, 123(26):16083–16090, 2019.

[71] Sara M Franzén, Linnéa Jönsson, Pau Ternero, Monica Kåredal, Axel C Eriksson, Sara Blomberg, Julia-Maria Hübner, and Maria E Messing. Compositional tuning of gas-phase synthesized pd–cu nanoparticles. *Nanoscale Advances*, 2023.

[72] Claudiu Bulbucan, Calle Preger, Aram Kostanyan, Kirsten MØ Jensen, Esko Kokkonen, Cinthia Piamonteze, Maria E Messing, and Rasmus Westerström. Large exchange bias in cr substituted fe 3 o 4 nanoparticles with feo subdomains. *Nanoscale*, 13(37):15844–15852, 2021.

[73] Claudiu Bulbucan, Pau Ternero, Calle Preger, Aram Kostanyan, Maria E Messing, and Rasmus Westerström. Cr-substituted fe304 nanoparticles: The role of particle size in the formation of fexo sub-domains and the emergence of exchange bias. *Journal of Magnetism and Magnetic Materials*, page 170359, 2023.

[74] Calle Preger, Niels C Overgaard, Maria E Messing, and Martin H Magnusson. Predicting the deposition spot radius and the nanoparticle concentration distribution in an electrostatic precipitator. *Aerosol Science and Technology*, 54(6):718–728, 2020.

[75] Thomas J Krinke, Knut Deppert, Martin H Magnusson, Frank Schmidt, and Heinz Fissan. Microscopic aspects of the deposition of nanoparticles from the gas phase. *Journal of Aerosol Science*, 33(10):1341–1359, 2002.

[76] Prithwish Biswas, Pankaj Ghildiyal, George W Mulholland, and Michael R Zachariah. Modelling and simulation of field directed linear assembly of aerosol particles. *Journal of Colloid and Interface Science*, 592:195–204, 2021.

[77] Namsoon Eom, Maria E Messing, Jonas Johansson, and Knut Deppert. General trends in core–shell preferences for bimetallic nanoparticles. *ACS nano*, 15(5):8883–8895, 2021.

[78] Klito C Petallidou, Pau Ternero, Maria E Messing, Andreas Schmidt-Ott, and George Biskos. Tuning atomic-scale mixing of nanoparticles produced by atmospheric-pressure spark ablation. *Nanoscale Advances*, 5(24):6880–6886, 2023.

[79] GW Qin, WL Pei, YP Ren, Y Shimada, Y Endo, M Yamaguchi, S Okamoto, and O Kitakami. Ni80fe20 permalloy nanoparticles: Wet chemical preparation, size control and their dynamic permeability characteristics when composited with fe micron particles. *Journal of magnetism and magnetic materials*, 321(24):4057–4062, 2009.

[80] Stefanos Mourdikoudis, Athanasia Kostopoulou, and Alec P LaGrow. Magnetic nanoparticle composites: synergistic effects and applications. *Advanced Science*, 8(12):2004951, 2021.

[81] Eckart F Kneller and Reinhard Hawig. The exchange-spring magnet: a new material principle for permanent magnets. *IEEE Transactions on Magnetics*, 27(4):3588–3560, 1991.

[82] T Hawa and MR Zachariah. Molecular dynamics simulation and continuum modeling of straight-chain aggregate sintering: Development of a phenomenological scaling law. *Physical Review B*, 76(5):054109, 2007.

[83] MJ Kirchhof, H-J Schmid, and W Peukert. Three-dimensional simulation of viscous-flow agglomerate sintering. *Physical Review E*, 80(2):026319, 2009.

[84] John MD Coey. *Magnetism and magnetic materials*. Cambridge university press, 2010.

[85] Bernard Dennis Cullity and Chad D Graham. *Introduction to magnetic materials*. John Wiley & Sons, 2011.

[86] Mario Norberto Baibich, Jean Marc Broto, Albert Fert, F Nguyen Van Dau, Frédéric Petroff, P Etienne, G Creuzet, A Friederich, and J Chazelas. Giant magnetoresistance of (001) fe/(001) cr magnetic superlattices. *Physical review letters*, 61(21):2472, 1988.

[87] Grünberg Binasch, Peter Grünberg, F Saurenbach, and W Zinn. Enhanced magnetoresistance in layered magnetic structures with antiferromagnetic interlayer exchange. *Physical review B*, 39(7):4828, 1989.

[88] S Ikeda, J Hayakawa, Y Ashizawa, YM Lee, K Miura, H Hasegawa, M Tsunoda, F Matsukura, and H Ohno. Tunnel magnetoresistance of 604% at 300k by suppression of ta diffusion in cofeb/ mgo/ cofeb pseudo-spin-valves annealed at high temperature. *Applied Physics Letters*, 93(8), 2008.

[89] Kay Yakushiji, Seiji Mitani, Franck Ernult, Koki Takanashi, and Hiroyasu Fujimori. Spin-dependent tunneling and coulomb blockade in ferromagnetic nanoparticles. *Physics reports*, 451(1):1–35, 2007.

[90] Michel Julliere. Tunneling between ferromagnetic films. *Physics letters A*, 54(3):225–226, 1975.

[91] Gerrit Van der Laan and Adriana I Figueroa. X-ray magnetic circular dichroism—a versatile tool to study magnetism. *Coordination Chemistry Reviews*, 277:95–129, 2014.

[92] Claas Abert. Micromagnetics and spintronics: models and numerical methods. *The European Physical Journal B*, 92:1–45, 2019.

[93] Jonathan Leliaert and Jeroen Mulkers. Tomorrow's micromagnetic simulations. *Journal of Applied Physics*, 125(18):180901, 2019.

[94] T Dion, DM Arroo, K Yamanoi, T Kimura, JC Gartside, LF Cohen, H Kurebayashi, and WR Branford. Tunable magnetization dynamics in artificial spin ice via shape anisotropy modification. *Physical Review B*, 100(5):054433, 2019.

[95] Hiroshi Tsukahara, Kaoru Iwano, Tadashi Ishikawa, Chiharu Mitsumata, and Kanta Ono. Large-scale micromagnetics simulation of magnetization dynamics in a permanent magnet during the initial magnetization process. *Physical Review Applied*, 11(1):014010, 2019.

[96] Thomas L Gilbert. A phenomenological theory of damping in ferromagnetic materials. *IEEE transactions on magnetics*, 40(6):3443–3449, 2004.

[97] Michael J Donahue and MJ Donahue. *OOMMF user's guide, version 1.0*. US Department of Commerce, National Institute of Standards and Technology, 1999.

[98] Marijan Beg, Martin Lang, and Hans Fangohr. Ubermag: Towards more effective micromagnetic workflows. *IEEE Transactions on Magnetics*, 58(2):1–5, 2022.

[99] Alfred Wiedensohler. An approximation of the bipolar charge distribution for particles in the submicron size range. *Journal of aerosol science*, 19(3):387–389, 1988.

Scientific Publications

Author Contributions

Co-authors and contributors are abbreviated as follows:
Rasmus Westerström (R.W.), Pau Ternero (P.T.), Claudiu Bulbucan (C.B.), Alexander Omelyanchik (A.O.), Pierfrancesco Maltoni (P.M.), Davide Peddis (D.P.), Maik Kahnt (M.K.)

Paper I: Template-free generation and integration of functional 1D magnetic nanostructures

I conceived the project together with R.W. I performed all the sample preparations, SEM imaging, electrical measurements, and micromagnetic simulations. I performed part of the STXM-XMCD imaging. I developed and carried out the idea of fabricating the devices by first making the contacts and then integrating nanoparticles onto them. XRD and TEM data acquisition were performed by P.T., and the magnetic data acquisition was carried out by P.M. and D.P. I analyzed all the data, wrote the manuscript, and made revisions based on feedback from my co-authors.

Paper II: Single-step generation of 1D FeCo nanostructures

I conceived the project together with R.W. I developed the concept of using identical-location SEM to monitor the self-assembly process and conducted the imaging. I prepared all the samples, performed the STXM-XMCD imaging, carried out the magnetic hysteresis measurements, and conducted the micromagnetic simulations. P.T. performed the XRD and TEM data acquisition. I analyzed all the data, wrote the manuscript, and made revisions based on feedback from my co-authors.

Paper III: Effect of the carrier gas on the structure and composition of Co–Ni bimetallic nanoparticles generated by spark ablation

I have been actively involved in sample preparation and data analysis.

Paper IV: Facile morphology and composition control of self-assembled structures by charged gas-phase magnetic nanoparticles

I conceived the project and demonstrated the possibility of controlling the spatial distribution of nanochains using an electric field. I prepared all the samples, conducted SEM imaging and analysis, performed nanoparticle deposition simulations, carried out STXM imaging, and handled all the data analysis. A.O. performed the magnetic field map measurements, P.T. did the TEM-XEDS data acquisition, and M.K. did the XRF microscopy. I wrote the entire manuscript.

Paper V: Single-step production and self-assembly of magnetic nanostructures for magneto-responsive soft films

I conceived the project and the idea of using the developed methodology for fabricating magnetically responsive soft films. I performed all the sample preparations, SEM imaging and analysis, magnetic film fabrication, most of the magnetic measurements, and analyzed all the data. Some of the magnetic data acquisitions were carried out by P.M. and D.P. I wrote the manuscript and made revisions based on feedback from my co-authors.

Paper VI: Direct device integration of single 1D nanoparticle assemblies; A magnetization reversal and magnetotransport study

I conceived the project together with R.W. I performed all the sample preparations, including the device fabrication, and carried out the SEM and the electrical measurements. I performed the STXM-XMCD measurements, and I developed scripts to analyze the microscopy results. I conceived and developed the new micromagnetic simulation methodology for nanoparticle assemblies. I wrote the manuscript and made revisions based on feedback from my co-authors.

Printed by Media-Tryck, Lund 2025 NORDIC SWAN ECOLABEL 3041 0903

Lund University
Faculty of Science
Department of Physics

ISBN 978-91-8104-519-2